Macrophages promote endothelial-to-mesenchymal transition via MT1-MMP/TGFβ1 after myocardial infarction

Running title: Macrophages and post-MI EndMT

Laura Alonso-Herranz[1], Álvaro Sahún-Español[2], Pilar Gonzalo[2], Polyxeni Gkontra[2], Vanessa Núñez[1], Marta Cedenilla[1], María Villalba-Orero[1], Javier Inserte[3,4], Cristina Clemente[2], David García-Dorado[3,4], Alicia G Arroyo[5]*, and Mercedes Ricote[1,6,*]

[1]Myocardial Pathophysiology Area, Centro Nacional de Investigaciones Cardiovasculares Carlos III (CNIC), 28029, Madrid, Spain

[2]Vascular Pathophysiology Area, Centro Nacional de Investigaciones Cardiovasculares Carlos III (CNIC), 28029, Madrid, Spain

[3]Cardiovascular Diseases Research Group, Vall d'Hebron University Hospital and Research Institute (VHIR), 08035, Barcelona, Spain

[4]CIBER de Enfermedades Cardiovasculares (CIBERCV), 28029, Madrid, Spain

[5]Centro de Investigaciones Biológicas Margarita Salas (CIB-CSIC), 28040, Madrid, Spain

[6]Lead contact: Mercedes Ricote (mricote@cnic.es)

*Corresponding authors: Alicia G Arroyo (agarroyo@cib.csic.es, +34 91 8373112 Ext. 4309) and Mercedes Ricote (mricote@cnic.es, +34 914531200 Ext. 3306)

ABSTRACT

Macrophages produce factors that participate in cardiac repair and remodeling after myocardial infarction (MI); however, how these factors crosstalk with other cell types mediating repair is not fully understood. In this study, we demonstrated that cardiac macrophages increased expression of *Mmp14* (MT1-MMP) 7 days post-MI. Specific macrophage-targeting of MT1-MMP (MT1-MMP$^{\Delta LysM}$ mice) attenuates post-MI cardiac dysfunction, reduces fibrosis, and preserves the cardiac capillary network. Mechanistically, we showed that MT1-MMP activates latent TGFβ1 in macrophages, leading to paracrine SMAD2-mediated signaling in endothelial cells and endothelial-to-mesenchymal transition (EndMT). Post-MI MT1-MMP$^{\Delta LysM}$ hearts contained fewer cells undergoing EndMT than their wild-type counterparts, and MT1-MMP-deficient macrophages showed a reduced ability to induce EndMT in co-cultures with endothelial cells. Our results demonstrate the contribution of EndMT to cardiac fibrosis and adverse remodeling post-MI and identify macrophage MT1-MMP as a key regulator of this process. The identified mechanism has potential as a therapeutic target in ischemic heart disease.

INTRODUCTION

Although the mortality rate from cardiovascular disease (CVD) has declined over the last 50 years, myocardial infarction (MI) continues to be one of the most lethal diseases worldwide, and many pathologies arise from adverse remodeling after cardiac injury (eg, heart failure and cardiac rupture) (Benjamin et al., 2017). Therefore, new strategies are urgently needed to improve cardiac repair and function after MI. MI is usually provoked by plaque rupture in a coronary artery, resulting in insufficient oxygen supply to the myocardium, which undergoes necrosis. The onset of MI triggers a cascade of events, including cardiomyocyte death, acute inflammation, angiogenesis, and scar formation (Frangogiannis, 2015). Cardiac healing is impaired by both excessive and insufficient expansion of macrophages (Mφs), prompting interest in the potential of Mφs as therapeutic targets for CVD (Dick et al., 2019; Panizzi et al., 2010; van Amerongen et al., 2007). Nonetheless, the exact Mφ phenotypes and mechanisms that might enhance tissue repair are not clearly defined.

We and others have shown that post-injury Mφs are distinct from resident cardiac Mφs (Bajpai et al., 2019; Dick et al., 2019; Walter et al., 2018). Monocytes and Mφs are sequentially mobilized from bone marrow (BM) and spleen to the infarcted myocardium (Nahrendorf et al., 2007; Swirski et al., 2009). During day 1 to day 4 after injury, Ly6C^{high} inflammatory Mφs clear necrotic cellular debris and damaged extracellular matrix (ECM) from the tissue and attract other immune cells through the secretion of pro-inflammatory cytokines (TNFα, IL1β, and IL6) that further fuel inflammation. Over the course of several days, the inflammatory phase gives

way to a healing phase, dominated by a second wave of Mφs, this time Ly6C^{low} reparative Mφs with the capacity to dampen inflammation and promote ECM reconstruction and angiogenesis. These latter Mφs are characterized by the secretion of anti-inflammatory (IL10), angiogenic (VEGF), and pro-fibrotic (TGFβ1) factors, as well as matrix metalloproteinases (MMPs), which promote tissue remodeling (Nahrendorf et al., 2007; Walter et al., 2018). However, how these factors produced by Mφs crosstalk with other cell types and orchestrate cardiac repair is still not-fully elucidated.

MMPs are a family of zinc-dependent endopeptidases that have been traditionally associated with the degradation and turnover of ECM components. MMPs are now known to directly and indirectly regulate cell behavior and microenvironment through the proteolytic processing of a large variety of molecules, such as membrane receptors and growth factors (Page-McCaw et al., 2007). Membrane type 1 matrix metalloproteinase (MT1-MMP/*Mmp14*) was the first membrane-anchored MMP to be described (Sato et al., 1994), and the cell surface location provides this enzyme with exclusive functions affecting cellular behavior. MT1-MMP is involved in the degradation of a spectrum of structural matrix proteins (including collagens I, II, and III, fibronectin, and laminin), the proteolytic processing of growth factors and cytokines (e.g., TGFβ and SDF-1), and the activation of other MMPs (e.g., pro-MMP2), expanding MT1-MMP functional pleiotropism.

Previous studies pointed out a deleterious role of MT1-MMP in post-MI cardiac remodeling, mostly related to its collagenase activity in fibroblasts (Koenig et al., 2012). Nevertheless, specific Mφ MT1-MMP contribution to cardiac healing response has never been addressed. In this study, we demonstrate that Mφ-restricted MT1-MMP deletion attenuates post-MI left ventricular (LV) dysfunction by preventing endothelial-to-mesenchymal transition (EndMT) and propose new treatment options for cardiac ischemic disease based on the modulation of Mφ MT1-MMP activity.

RESULTS

MI induced the expression of *Mmp14* in Mφs

To gain insight into the potential contribution of Mφ-produced MT1-MMP to cardiac healing, we induced MI in adult mice by permanent coronary ligation (LAD-ligation). Using an established gating strategy (Walter et al., 2018), we isolated cardiac Mφs at 0, 3, 7 and 28 days post-MI (Figure 1- Figure supplement 1A-B) and assessed gene expression related to ECM remodeling (Figure 1A). MI induced expression of *Mmp14* (MT1-MMP) and its substrates *Mmp2* and *Col1a1* in Mφs in the heart, reaching maximum levels of expression on day 7 post-MI. In contrast, other MMP family members (*Mmp9* and *Mmp13*) were downregulated after infarction.

Mφ-restricted MT1-MMP deficiency attenuates LV dysfunction and dilation and reduces collagen deposition after MI

To explore the role of Mφ-derived MT1-MMP in post-MI LV function and remodeling, we generated a Mφ-specific KO mouse for *Mmp14*. LysM-Cre mice (Clausen et al., 1999) were crossed with MT1-MMP$^{f/f}$ mice (Gutierrez-Fernandez et al., 2015), resulting in the deletion of exons 4 and 5 in the floxed *Mmp14* allele in MT1-MMP$^{\Delta LysM}$ mice (Cre^{+} mice) (Figure 1- Figure supplement 2A). MT1-MMP$^{f/f}$ littermates (Cre^{-}) were used as controls. No significant differences in either baseline cardiac function (Table 1) or in circulating monocytes and neutrophils were found between genotypes (Table 2, and Figure 1- Figure supplement 2B-C). *Mmp14* was efficiently deleted in BM-derived Mφs (BMDMs) and in cardiac Mφs sorted from 7-day-post-MI MT1-MMP$^{\Delta LysM}$ hearts; in contrast, *Mmp14* expression did not differ between ECs purified from MT1-MMP$^{f/f}$ and MT1-MMP$^{\Delta LysM}$ 7-day-post-MI hearts (Figure 1- Figure supplement 2D). The low efficiency recombination of LysM-Cre system in monocytes and dendritic cells (Abram et al., 2014) and the lack of MT1-MMP expression in neutrophils (Daseke et al., 2019) make MT1-MMP$^{\Delta LysM}$ mouse a suitable model to study Mφ-MT1-MMP role in post-MI LV remodeling and function.

Echocardiography revealed that Mφ-deletion of MT1-MMP ameliorated LV dysfunction and prevented LV dilation post-MI, with MT1-MMP$^{\Delta LysM}$ mice having a significantly higher LV ejection fraction (LVEF) and lower LV end-diastolic volume (LVVold) (Figure 1B-C, and Video 1). Infarct size and LV wall motion score index (WMSI) were calculated to assess global and regional cardiac contractility abnormalities by echocardiography (see Materials and Methods). This analysis showed that LAD-ligation produced smaller infarcts and a lower WMSI in MT1-MMP$^{\Delta LysM}$ mice (Figure 1D-E), indicating better preservation of cardiac function and less pronounced wall-motion abnormalities in the LV when Mφ MT1-MMP was absent.

MT1-MMP can process a variety of ECM components, so we next analyzed the fibrotic response to MI. Transverse sections of 28-day-post-MI hearts were assessed using a multi-photon laser scanning microscope to capture multi-photon autofluorescence (MPEF) and second harmonic generation (SHG) signals, allowing simultaneous visualization of myocyte components and fibrillary collagen, respectively. SHG images of the infarct zone (IZ) revealed a highly directional and organized collagen fibril morphology in the MT1-MMP$^{f/f}$ infarcted group, whereas a less-organized and sparse collagen structure was observed in MT1-MMP$^{\Delta LysM}$ infarcted hearts (Figure 1F). Quantification of SHG signals revealed a marked drop in fibrillary collagen density in MT1-MMP$^{\Delta LysM}$ infarcted hearts (Figure 1G). In addition, the analysis of first-order features of collagen fibrils in SHG images showed augmented skewness and kurtosis in MT1-MMP$^{\Delta LysM}$ mice, indicating thinner and underdeveloped, disarrayed collagen fibers and thus lower tissue stiffness (Figure 1G).

We next investigated the effect of Mφ-specific MT1-MMP deletion during transient ischemia/reperfusion (I/R) model of MI. Similar to the permanent occlusion model, transient ischemia impaired LV function in both genotypes, but MT1-MMP$^{\Delta LysM}$ mice had a significantly higher LVEF and lower LV end-systolic and end-diastolic internal diameters (LVIDs and LVIDd, respectively), indicating better preserved LV function and prevention of LV dilation (Figure 1- Figure supplement 3A). Moreover, SHG imaging analysis after I/R revealed a weaker fibrotic response, with thinner and sparser collagen fibers in MT1-MMP$^{\Delta LysM}$ hearts (Figure 1- Figure supplement 3B-C).

These data indicate that Mφ MT1-MMP-deficiency decreases collagen fiber deposition, producing a smaller and underdeveloped fibrotic scar that results in relatively low LV dilation and ameliorated systolic dysfunction after transient or permanent cardiac ischemia.

MT1-MMP$^{\Delta LysM}$ mice have a preserved microvasculature network and better myocardial oxygenation after ischemic injury

Confocal images of MT1-MMP$^{f/f}$ and MT1-MMP$^{\Delta LysM}$ 7-day-post-MI hearts stained for CD31 (endothelial marker) and SMA (smooth muscle actin) were evaluated with a fully automated 3D pipeline (Materials and Methods), which allows reconstruction and quantification of the microvasculature (Gkontra et al., 2018b) (Table 3). MT1-MMP$^{\Delta LysM}$ 7-day-post-MI hearts had a higher vascular volume density and more capillaries and ECs within the infarction than controls (Figure 2A-B). Oxygen diffusion from blood to tissue critically depends on the density and arrangement of the microvascular bed. Accordingly, in MT1-MMP$^{\Delta LysM}$ hearts, we observed increased capillary density and reduced intercapillary and diffusion distances, parameters proposed as indices of oxygen diffusion (Gkontra et al., 2018b), suggesting better oxygen diffusion in the infarcted myocardium (Figure 2B). We next assessed hypoxia in the post LAD-ligation myocardium by carbonic anhydrase IX (CA-IX) staining (Figure 2C), which revealed a smaller CA-IX+ area in the infarction of 7-day-post-MI MT1-MMPΔLysM hearts than in controls (Figure 2C-D), confirming better preserved tissue oxygenation after MI. No hypoxia signal was found in the non-infarcted tissue (Figure 2- Figure supplement 1A-B). Although there were no between-genotype differences in arteriole (SMA^{+} vessels) density, there was a trend toward thinner arteriole vessel walls at 7 days post-MI in MT1-MMP$^{\Delta LysM}$ infarcted hearts (Figure 2- Figure supplement 1C-D), suggesting amelioration of MI-induced arterial hyperplasia (Krishnamurthy et al., 2009) in the absence of Mφ MT1-MMP.

The absence of Mφ MT1-MMP impairs active TGFβ1 release from LAP-TGFβ1 complex

To elucidate the mechanism by which Mφ MT1-MMP regulates microvascular density and fibrosis, we sought soluble factors whose release might be affected by MT1-MMP. Two

independent proteomics studies previously performed in our laboratory detected a 1.25- to 2-fold increase in TGFβ1 content in the membrane-enriched subcellular fraction of MT1-MMP$^{-/-}$ BMDMs. The small latent complex (SLC) consisting of latency associated peptide (LAP) and mature TGFβ1 can be retained at the cell surface through LAP binding to membrane receptors (e.g. integrin αvβ8) (Figure 3A). It has been shown that MT1-MMP promotes TGFβ1 activation via integrin αvβ8 at the cell surface (Mu et al., 2002), and that TGFβ1 modulates myocardial healing through effects on the fibrotic and angiogenic responses (Frangogiannis, 2020).

To investigate the possible role of Mφ-derived MT1-MMP in TGFβ1 release after MI, we used flow cytometry to measure latent TGFβ1 (LAP-TGFβ1 complex) on the surface of LPS-stimulated MT1-MMP$^{f/f}$ and MT1-MMP$^{\Delta LysM}$ BMDMs (Figure 3A-C). MT1-MMP$^{\Delta LysM}$ Mφs had a higher content of LAP and TGFβ1, revealing significantly higher surface retention of LAP-TGFβ1 than observed in WT Mφs (Figure 3B-C). To validate this observation, we detected TGFβ1 by immunoblot in membrane and cytosolic subcellular fractions and total cell lysates of LPS-stimulated MT1-MMP$^{f/f}$ and MT1-MMP$^{\Delta LysM}$ BMDMs (Figure 3D). Latent TGFβ1 (~50 kDa) consisting of LAP (35 kDa) covalently bound to the mature TGFβ1 (12.5 kDa) preferentially located in the membrane and was more abundant in MT1-MMP$^{\Delta LysM}$ Mφs (Figure 3C-D). In line with the reported role of MT1-MMP in posttranslational processing of pro-TGFβ1, we found no difference in *Tgfb1* transcript levels between MT1-MMP$^{Lf/f}$ and MT1-MMP$^{\Delta LysM}$ BMDMs (Figure 3E).

We next queried whether impaired processing of LAP-TGFβ1 complex by MT1-MMP-deficient Mφs affects secretion of active TGFβ1. Since active TGFβ1 has an estimated half-life of 2-3 minutes, and only 2%-5% of total TGFβ1 is thought to be activated at any given time (Lawrence, 2001), we measured bioactive TGFβ1 using a standardized luciferase assay (Materials and Methods). Responsiveness of the luciferase construct to TGFβ1 was confirmed by treating transfected HEK293 cells with TGFβ1 (2.94 ± 0.06 fold-increase in arbitrary luciferase units (ALU) with respect to the control). Luciferase activity was then assessed in transfected HEK293 cells cultured in the presence or absence of LPS-stimulated BMDMs for 24 h (Figure 3F). HEK293 co-culture with MT1-MMP$^{f/f}$ BMDMs produced abundant levels of active TGFβ1, whereas active TGFβ1 was undetectable after co-culture with MT1-MMP$^{\Delta LysM}$ BMDMs (Figure 3F). TGFβ1 levels in KO BMDMs were restored by transduction with full-length (FL) MT1-MMP but not with a catalytic mutant (E240A), demonstrating that MT1-MMP-dependent TGFβ1 activation requires MT1-MMP catalytic activity (Figure 3G).

The absence of Mφ MT1-MMP reduces TGFβ1-pSMAD2 signaling in cardiac ECs, MyoFBs, and VSMCs after MI

We explored if defective release of active TGFβ1 by MT1-MMP-deficient Mφs could affect TGFβ1-mediated SMAD2/3 in the myocardium. We quantified phosphorylated SMAD2 (pSMAD2) in Mφs, ECs and MyoFBs by flow cytometry in 7-day-post-MI hearts (Figure 4A-B). Mφs were defined as $CD45^+CD11b^+F4/80^+$ cells, and ECs as $CD45^-CD31^+$ cells (Figure 4A). Cardiac fibroblast convert to MyoFBs with injury to mediate healing after MI and platelet-derived growth factor receptor β (PDGFRβ) induction is an early feature of MyoFB activation (Henderson et al., 2013). PDGFRβ is also expressed by VSMCs (Gkontra et al., 2018b). Therefore, MyoFBs and VSMCs were described as $CD45^-CD31^-PDGFR\beta^+$ cells (Figure 4A). MyoFBs also express other classic fibroblast-associated markers as *Cdh2, Col1a1, Col1a2, Col1a3* (Figure 5- Figure supplement 1A-B). There was no between-genotype difference in pSMAD2 abundance in Mφs; however, pSMAD2 was significantly less abundant in ECs and MyoFBs/VSMCs from MT1-$MMP^{\Delta LysM}$ hearts (Figure 4B-C), suggesting that lack of Mφ MT1-MMP impairs paracrine TGFβ1-pSMAD2 signaling in ECs and MyoFBs/VSMCs. To distinguish between pSMAD2 in MyoFBs (non-vascular-related SMA^+ cells) and VSMCs (vascular-related SMA^+ cells), we performed confocal imaging analysis at 7 days post-MI which revealed that pSMAD2-positive MyoFBs and VSMCs were both less abundant in MT1-$MMP^{\Delta LysM}$ hearts than in MT1-$MMP^{f/f}$ hearts (Figure 4D-E).

Mφ-derived MT1-MMP induces EndMT after MI

We found that Mφ MT1-MMP deletion altered the cellular composition of the infarcted myocardium, with MT1-$MMP^{\Delta LysM}$ mice showing fewer Mφs, indicating a less inflammatory state; more ECs, in line with the microvasculature image analysis data; and fewer MyoFBs, in agreement with the reduced fibrotic response (Figure 5A-B). Additionally, we detected an intermediary population of cells with mild levels of both CD31 (endothelial marker) and PDGFRβ (mesenchymal marker) (Figure 5A). This population is suggestive of transitioning cells undergoing endothelial to mesenchymal transition (EndMT) (Aisagbonhi et al., 2011). To confirm the occurrence of EndMT in the context of MI, we performed lineage tracing experiments in Cdh5-Cre^{ERT2} R26Tomato control and infarcted mice and asked whether we could find endothelial-cell derived $Tomato^+$ cells within the MyoFB compartment using flow cytometry (Figure 5- Figure supplement 2A-E). We detected an increase in $Tomato^+PDGFR\beta^+$ cells in 7-day-post-MI hearts (Figure 5- Figure supplement 2D, E), confirming that EndMT is triggered upon MI as previously reported (Aisagbonhi et al., 2011). We confirmed the transitioning phenotype of $CD31^+PDGFR\beta^+$ cells by qPCR and observed the loss of endothelial markers (i.e. *Pecam, Cdh5, Kdr, Tie2, Col4a2*), the acquisition of mesenchymal genes (i.e. *Cdh2, Tagln, Col1a1, Col1a2, Col3a1*), and the upregulation of EndMT-mediating transcriptional factors (i.e. *Zeb2* and *Snai1*) (Figure 5- Figure supplement 1A-B). Interestingly, these cells were less abundant in Mφ-MT1-MMP deficient hearts (Figure 5A-B), suggesting

that EndMT is impaired in the absence of Mφ MT1-MMP. We confirmed the results obtained with PDGFRβ staining by the complementary staining for MEFSK4 (Figure 5- Figure supplement 3A, B), another marker for cardiac fibroblasts (Pinto et al., 2016).

TGFβ is considered the master mediator of EndMT, in a SMAD-dependent manner (Frangogiannis, 2020). We found by immunofluorescence triple positive cells for the endothelial nuclear marker ERG, the mesenchymal marker SMA and pSMAD2, reflecting the transition of endothelial cells towards a mesenchymal phenotype via SMAD2 activation in the infarcted cardiac tissue (Figure 5- Figure supplement 3C-D). We therefore studied the effect on post-MI EndMT of the impaired TGFβ1 production by MT1-MMP-deficient Mφs, and the associated reduction in paracrine pSMAD2 signaling in ECs. For that, we co-cultured purified MAECs with LPS-activated MT1-MMP$^{f/f}$ or MT1-MMP$^{\Delta LysM}$ BMDMs (Figure 6- Figure supplement 1). Immunofluorescence analysis with the endothelial marker CD31 and the mesenchymal marker SMA revealed morphological changes in MAECs after co-culture with MT1-MMP$^{f/f}$ BMDMs, with cells progressively losing their cobblestone appearance and adopting a dispersed, spindle-shaped morphology (Figure 6- Figure supplement 1A). Moreover, MAECs co-cultured with MT1-MMP$^{f/f}$ BMDMs significantly decreased CD31 expression and acquired SMA expression, indicating the acquisition of molecular traits of a mesenchymal phenotype (Figure 6- Figure supplement 1A-B). This phenotype was similar to the effects of recombinant TGFβ1 stimulation (Figure 6- Figure supplement 1A-B). In contrast, co-culture of MAECs with MT1-MMP$^{\Delta LysM}$ BMDMs led neither to the loss of endothelial features nor to the acquisition of mesenchymal markers (Figure 6- Figure supplement 1A-B). Altered expression of endothelial and mesenchymal markers in the co-cultures was confirmed by qPCR. In accordance with the immunofluorescence data, the co-culture of MAECs with MT1-MMP$^{f/f}$ BMDMs caused the downregulation of EC-related genes (*Pecam*, *Kdr*, and *Col4a2*) and the upregulation of mesenchymal genes (*Tagln* and *Acta2*) and the direct TGFβ1 target *Pai1*. A similar phenotype was induced by TGFβ1-treatment. In contrast, these changes toward a mesenchymal phenotype in MAECs were not triggered by co-culture with MT1-MMP$^{\Delta LysM}$ BMDMs (Figure 6- Figure supplement 1C).

To confirm Mφ MT1-MMP-dependent induction of EndMT *in vivo* following MI, we first investigated TGFβ1 processing in cardiac Mφs. LAP and TGFβ1 were both significantly increased on the surface of MT1-MMP$^{\Delta LysM}$ Mφs after MI, indicating the retention of latent TGFβ1 (Figure 6A). We then sorted cardiac Mφs from 7-day-post-MI MT1-MMP$^{f/f}$ and MT1-MMP$^{\Delta LysM}$ hearts (Figure 1- Figure supplement 1A-B) and co-cultured them with luciferase-transfected HEK293 cells. As with BMDMs, post-MI WT cardiac Mφs produced detectable levels of active TGFβ1, whereas the deletion of Mφ MT1-MMP abrogated TGFβ1 activation (Figure 6B). In co-culture experiments, MT1-MMP$^{f/f}$ cardiac Mφs induced EndMT in MAECs,

downregulating CD31 expression and increasing SMA expression. In contrast, no transition to a mesenchymal phenotype was evident in MAECs co-cultured with MT1-MMP-deficient cardiac Mφs (Figure 6C-D).

DISCUSSION

MI results in loss of cardiomyocytes, adverse structural remodeling, and LV dysfunction and dilation, eventually causing heart failure. Since appropriate cardiac repair requires a balanced inflammatory response to avoid adverse cardiac remodeling after MI, Mφs have emerged as likely candidates for investigation and therapeutic intervention. Our results show that post-MI Mφs have heightened expression of *Mmp14* as well as its substrates *Mmp2* and *Col1a1*, in line with a role in tissue remodeling and collagen deposition (O'Rourke et al., 2019). Although ECM remodeling and granulation tissue formation are prerequisites for tissue repair, excessive MMP activity after MI and subsequent ECM turnover can result in adverse remodeling and worsened cardiac dysfunction (Spinale et al., 2010). Therefore, we hypothesized that Mφ-specific deletion of MT1-MMP might limit adverse remodeling and LV dilation and dysfunction after MI.

Although MT1-MMP$^{\Delta LysM}$ mice are phenotypically normal under homeostatic conditions, these animals were protected when challenged by acute MI. MT1-MMP$^{\Delta LysM}$ mice had smaller infarcts and better LV contractility after MI than controls, as well as significantly improved preservation of systolic function and LV structure. A detrimental role of MT1-MMP in post-MI cardiac remodeling has been identified using mouse infarct models, leading to worsening cardiac function and reduced survival (Koenig et al., 2012; Spinale et al., 2010; Zavadzkas et al., 2011). These studies attributed this detrimental role to MT1-MMP collagenase activity in fibroblasts, disregarding its actions in Mφs (Koenig et al., 2012). Our data obtained with the MT1-MMP$^{\Delta LysM}$ model are the first demonstrating the beneficial effect of Mφ-specific MT1-MMP deletion in preventing adverse LV remodeling after MI. This effect is likely caused by the lower myocardial fibrosis, allowing the heart to work at less of a mechanical disadvantage, and better oxygenation of the infarcted myocardium due to the preservation of the microvasculature network.

Loss of collagenase activity in MT1-MMP$^{\Delta LysM}$ mice might be expected to lead to a dense scar. However, in addition to its collagenolytic activity (Ohuchi et al., 1997), MT1-MMP proteolytically processes a diverse range of biologically active signaling molecules (Koziol et al., 2012); stimulation of collagen synthetic pathways by these molecules would explain the observed phenotype of post-MI MT1-MMP$^{\Delta LysM}$ mice. Pro-TGFβ has been recognized as a target for MT1-MMP–mediated cleavage in several contexts (Koziol et al., 2012; Mu et al., 2002). Our results provide evidence for MT1-MMP-mediated activation of latent LAP-TGFβ1

complex in cardiac Mφs after MI. Dampened processing and release of active TGFβ1 in MT1-MMP$^{\Delta LysM}$ mice was associated with a decrease in SMAD2-mediated signaling in the infarcted myocardium, providing a mechanism for the reduced pro-fibrotic response and preservation of microvasculature network. Previous studies identified MT1-MMP as an inducer of fibrosis through its cleavage of latent-transforming growth factor beta-binding protein 1 (LTBP1) and activation of TGFβ-mediated SMAD2/3 signaling in the infarcted myocardium (Spinale et al., 2010; Zavadzkas et al., 2011). Suppressed TGFβ1 production could also underlie the preservation of the microvasculature network in MT1-MMP$^{\Delta LysM}$ mice, through the loss of TGFβ1 angiostatic effects (Arnold et al., 2014; Imaizumi et al., 2010).

TGFβ-mediated EndMT has been identified during cardiac fibrosis (Zeisberg et al., 2007), contributing to collagen matrix deposition and disease. The concomitant loss of functional ECs may also lead to capillary rarefaction, thus causing tissue ischemia, a potent driver of fibrosis. EndMT is essential for cardiac valve formation and vascular development in embryogenic stages as well as in the pathogenesis of diverse cardiovascular disorders, such as congenital heart disease (Hofmann et al., 2012; Xu et al., 2015). The contribution of EndMT to cardiac fibrosis remains however a matter of debate, which depends on the nature of the cardiovascular injury and the extent of the fibrosis (Aisagbonhi et al., 2011; Evrard et al., 2016; Kanisicak et al., 2016; Moore-Morris et al., 2014; Zeisberg et al., 2007). For example, EndMT is minimal in pressure overload or I/R models, where the intensity of inflammatory and fibrotic responses is much lower than after acute ischemic injury (Moore-Morris et al., 2014; Xia et al., 2009). Besides, the tools employed for assessing EndMT present several limitations; for instance, immunofluorescence techniques are not sensible enough to reliably detect and quantify dim levels of protein expression that characterize cells under EndMT transition. Lineage tracing experiments are a preferable approach, although the specificity of the driver represents also a caveat (Kovacic et al., 2019; Li et al., 2018; Piera-Velazquez and Jimenez, 2019).

Our results using flow cytometry, a technique that allowed us to finely track shifts in the expression of markers associated to EndMT, showed changes in ECs, 'transitioning cells', and MyoFBs that demonstrate a role of Mφ-derived MT1-MMP in TGFβ1-mediated EndMT after MI, contributing to the observed phenotype. This conclusion is further supported by the identification of ERG^{+}SMA^{+} cells with active SMAD2 signaling pathway within the infarction and by the results obtained in *in vitro* experiments. Our findings are in line with the role of MT1-MMP as an activator of epithelial to mesenchymal transition (EMT) in other pathophysiological contexts such as development, cancer, and lung fibrosis (Garmon et al., 2018; Nguyen et al., 2016; Xiong et al., 2017). Interestingly, a recent scRNAseq study carried out on healthy and post-infarcted hearts identified a subset of post-MI Mφs with a HIF1α-

dependent signature, which specifically upregulated *Mmp14* expression (Dick et al., 2019). *Mmp14* expression in these cells converge with a hypoxia-driven program, which represents a well-known stimulus for EndMT (Evrard et al., 2016), further supporting the implication of *Mmp14*-expressing post-MI Mφs in EndMT. Moreover, Mφs have recently been reported as inducers of EndMT in atherosclerosis (Helmke et al., 2019).

Based on our discoveries, we propose that MT1-MMP mediated TGFβ1-activation in Mφs after ischemic injury triggers local EndMT and generation of MyoFBs during granulation tissue formation. These cells might then take part in fibrosis, giving rise to a dense fibrotic scar that compromises LV cardiac function after MI. Restraining Mφ-mediated TGFβ1 activation by MT1-MMP thus limits EndMT, favoring preservation of cardiac microvasculature, improving myocardial blood flow, and reducing tissue hypoxia and fibrotic scarring (Figure 7). These alterations in MT1-MMP$^{\Delta LysM}$ mice limited LV dilation and dysfunction and suggest novel approaches to the promotion of cardiac recovery after MI. Therapeutic strategies would consist of manipulating Mφ MT1-MMP production in order to control EndMT, thus promoting angiogenesis and moderating scar formation. Interestingly, in an experimental rat model of MI, treatment with menstrual-blood–derived mesenchymal stem cells has been shown to protect endothelial function, reduce infarct size, decrease cardiac fibrosis, and downregulate TGFβ1/SMAD signaling, all through the comprehensive inhibition of EndMT (Zhang et al., 2013). Following this rationale, previous studies have pointed to the beneficial effect of pharmacological inhibition of MMPs on post-MI cardiac remodeling; however, implementation of clinically relevant therapies has proved difficult (Creemers et al., 2001; Hudson et al., 2006; Yabluchanskiy et al., 2013). A recent study reported that selective MT1-MMP inhibition rescued tissue damage and mortality in influenza-infected mice, demonstrating the potential of specific MT1-MMP inhibitors to ameliorate the detrimental effects of this protease on tissue remodeling (Talmi-Frank et al., 2016). Controlling dysregulated myocardial MT1-MMP activity in Mφs could be a suitable option for patients at risk of developing heart failure after MI.

MATERIAL AND METHODS

Mice

All the animals used in this study were on the C57BL/6 background. Experiments were performed in 8- to 12-week-old both male and female mice, unless otherwise indicated, kept in a specific pathogen-free (SPF) facility at Centro Nacional de Investigaciones Cardiovasculares Carlos III (CNIC) under a 12 h light/dark cycle (lights on from 07:00 to 19:00 h), with water and chow available *ad libitum.* All animal procedures were conducted in accordance with EU Directive 86/609/EEC and approved by the Animal Subjects Committee of the Instituto de Salud Carlos III (Madrid, Spain) and Madrid Community Organs in the

PROEX 188/26. Animals used in this study were C57BL/6 mice (Charles River), LysMCre mice (Clausen et al., 1999), and *Mmp14*$^{f/f}$ mice (Gutierrez-Fernandez et al., 2015). LysM-Cre^{+}/*Mmp14*$^{f/f}$ mice (MT1-MMP$^{\Delta LysM}$) lack MT1-MMP in Mφs; while LysM-Cre^{-}/*Mmp14*$^{f/f}$ littermates (MT1-MMP$^{f/f}$) were used as WT controls. For endothelial lineage tracing experiments, we used Cdh5-Cre^{ERT2} mice (Wang et al., 2010) crossed with R26TdTomato mice (Madisen et al., 2010). Tamoxifen (Sigma-Aldrich) was dissolved in corn oil (15 mg / ml) and injected intraperitoneally (0.15 mg tamoxifen / g mouse body weight) 5 days before LAD-ligation surgery.

Mouse models of MI

1. Left anterior descending coronary artery ligation (LAD-ligation)

Permanent ligation of the left anterior descendent (LAD) coronary artery was performed as previously described (Kolk et al., 2009). Briefly, mice were anesthetized with sevoflurane (5% for induction, 2%-3% for maintenance), and intubated using a 24-gauge intravenous catheter with a blunt end. Mice were artificially ventilated with a mixture of O_2 and air [1:1 (vol/vol)] using rodent ventilator (minivent 845) with 160 strokes/min in a total volume of 250 µl. The mouse was placed on heating pad to maintain body temperature at 37°C. A thoracotomy was performed through the fourth left intercostal space, the pericardium was opened, and the heart was exposed. The proximal LAD coronary artery was permanently ligated with 7/0 silk suture (Lorca Marín). The thorax and the skin incision were closed with 6/0 silk sutures (Lorca Marín) and buprenorphine (0.01 mg/kg, Buprex, Merck & Co. Inc) was given for pain relief. Mice were sacrificed by CO_2 inhalation 3, 7, or 28 days post-MI. Animals not subjected to surgery were included as the physiological condition (day 0).

2. Ischemia-reperfusion (I/R)

I/R protocol was performed as previously described (Inserte et al., 2019), following the same anesthetic and thoracotomy protocol as in permanent LAD-ligation. Once the heart was exposed, the LAD coronary artery was ligated approximately 1 mm below the edge of the left atrial appendage with an 8/0 silk suture (EthiconEndo-surgery, OH, USA). Regional ischemia was verified by visual pallor and QRS alterations within the first seconds of occlusion. After occlusion for 45 min, the suture was loosened to start reperfusion. The thorax and the skin incision were closed with 6/0 silk sutures (Lab Arago, Spain) and buprenorphine (0.01 mg/kg, Buprex, Merck & Co. Inc) was given for pain relief. Mice with lack of ST-elevation during ischemia or lack of ST-recovery at reperfusion were excluded from further evaluation. Mice were sacrificed by CO_2 inhalation 21 days post-MI. Animals not subjected to surgery were included as the physiological condition (day 0).

For the two models of MI, mice with less than two affected LV segments after the surgery in terms of contractility were considered non-properly infarcted and excluded from the study.

Echocardiographic analysis

Transthoracic echocardiography was performed on mice subjected to LAD-ligation or I/R at basal, 7, and 21 or 28 days post-surgery. Shaved mice were anesthetized by inhalation of isoflurane and oxygen (1.25% and 98.75%, respectively) and placed in a biofeedback warming station that maintained core body temperature. Anesthesia depth was adjusted to maintain heart rate between 450 and 550 beats per minute. Warm ultrasound gel was applied to the chest of the animals, and echocardiography measurements were obtained using the VEVO 2100 high frequency ultrasound system with a linear transducer MS400 18–38 MHz (Visual Sonics, Toronto, Canada). Parasternal long- and short- axis views at 3 levels (base, middle and apex) in two-dimensional and M-mode were obtained as described previously (Cruz-Adalia et al., 2010). The LV end-systolic and end-diastolic volume (LVVols and LVVold, respectively) were acquired from the parasternal two-dimensional long-axis view, and LV ejection fraction (LVEF) was calculated using the area-length method (Ram et al., 2011). Wall thickness at the end of the systole and diastole was measured from the M-mode short-axis view. Analysis was performed off-line by two blinded echocardiography experts. Ultrasounds were performed in collaboration with Dr. María Villalba-Orero at CNIC.

Regional kinetic abnormalities within the LV were assessed. LV wall motion score index (WMSI) was calculated in order to assess global and regional cardiac function by a 12-based segment model, considering parasternal two-dimensional short and long axis views at the 3 levels, as previously described (Gallego-Colon et al., 2016). In each level, the LV was further divided in 4 segments (anterior, lateral, posterior, and septal) and every segment was scored according its severity in terms of contraction as 1 (normal), 2 (hypokinesia), 3 (akinesia), 4 (dyskinesia or aneurysm). Infarct size was estimated as the percentage of individual segments scored > 1 (reflecting contractility abnormalities) over the total of LV segments, and WMSI was defined as the ratio of the sum of the score of every segment over the total number of segments evaluated.

Flow cytometry and cell sorting

Cardiac single-cell suspensions were obtained as previously described (Alonso-Herranz et al., 2019). Briefly, mice were euthanized by CO_2 fixation and immediately perfused by intracardiac injection of cold PBS. Right and left atria were removed and the whole ventricles were minced with fine scissors and digested in collagenase IV 0.1% (528 U/mg Sigma) in PBS at 37°C for 45 minutes under gentle shaking. Cells were then filtered through

nylon mesh of 100 µm (BD biosciences) to obtain a homogeneous cell suspension and were subjected to red blood cells lysis with RBC Lysis buffer solution (eBioscience). Single cell suspensions were Fc-blocked using anti-mouse CD16/CD32 antibody (BD Pharmingen) 10 minutes at 4º C in FACS buffer (PBS 2% FBS 5mM EDTA). Antibodies were incubated for 30 minutes at 4º C in FACS buffer. Where appropriate, cells were further incubated with streptavidin conjugates for 30 minutes at 4º C. For nuclear pSMAD2 staining, cells were fixed and permeabilized using a commercial kit (Foxp3/Transcription Factor Staining Buffer Set, eBioscience). Flow cytometry studies were performed in a BD FACSCantoTM II flow cytometer (BD BioSciences) and analyzed with FlowJo Software (Tree Star). Cell sorting was performed with BD FACS-ARIATM II cell sorter (BD Biosciences).

After pre-selection in side scatter (SSC) *versus* forward scatter (FSC) dot plot to exclude debris and doublets, cardiac Mφs were identified as $CD45^+CD11b^+F4/80^+$ cells, ECs as $CD45^-CD31^+PDGFR\beta^-$ cells, 'transitioning' cells as $CD45^-CD31^{low}PDGFR\beta^{low}$ cells, and VSMCs and MyoFBs as $CD45^-CD31^-PDGFR\beta^+$ cells. Within the $CD45^+CD11b^+$ cells, the $F4/80^+Ly6C^{low}$ cardiac Mφs were sorted at 0, 7, and 28 days post-MI, whereas $F4/80^+Ly6C^{high}$ cardiac Mφs were purified for 3 days post-MI.

Fluorescence minus one (FMO) controls were included during acquisition for gating analyses to distinguish positive from negative staining cell populations. The standardized median fluorescence intensity (MFI) of TGFβ1, LAP and pSMAD2 for each cardiac cell type was calculated as previously described (Maecker et al., 2004):

$$\text{Standardized MFI} = \frac{(\text{median}_{\text{positive}} - \text{median}_{\text{FMO}})}{2*\text{SD}_{\text{FMO}}}$$

Whereas $median_{positive}$ is the median intensity of the positive cell population, $median_{FMO}$ is the median intensity of the FMO, and SD_{FMO} is the standard deviation of the intensity of the FMO.

List of antibodies used for flow cytometry

Antibody	Concentration	Provider	Reference
CD16/CD32 Rat Anti-Mouse	1:100	BD Biosciences	553141
CD45-PerCP/Cy5.5 Rat Anti-Mouse	1:100	Biolegend	103132
CD45-APC/Cy7 Rat Anti-Mouse	1:100	Biolegend	103116
CD45-eFluor 450 Rat Anti-Mouse	1:100	eBioscience	48-0451
CD11b-PE-Cy7 Rat Anti-Mouse	1:100	BD Biosciences	552850

CD11b-Biotin Anti-Mouse	1:100	BD Biosciences	51-017125
CD11b-FITC Rat Anti-Mouse	1:100	Biolegend	101206
Ly6C-APC Rat Anti-Mouse	2:100	BD Biosciences	560595
Ly6C-FITC Rat Anti-Mouse	1:100	AbD Serotec	553104
CD31-APC Rat Anti-Mouse	1:100	BD Biosciences	551262
CD31-FITC Rat Anti-Mouse	1:100	BD Biosciences	553372
PDGFR-β-PE Rat Anti-Mouse	2:100	BioLegend	136005
PDGFR-β-APC Rat Anti-Mouse	2:100	BioLegend	136007
MEFSK4-PE Rat Anti-Mouse	2:100	Miltenyi	130-120-166
MEFSK4-APC Rat Anti-Mouse	2:100	Miltenyi	130-120-802
F4/80-PE/Cy7 Rat Anti-Mouse	3:100	BioLegend	123114
F4/80-PE Rat Anti-Mouse	3:100	BioLegend	123110
Phospho-Smad2 (Ser245/250/255) Rabbit Anti-Mouse	1:100	Cell Signaling	3104
Streptavidin-Alexa 488 conjugate	1:500	ThermoFisher Scientific	S11223
LAP-APC Mouse Anti-Mouse	3:100	Biolegend	141405
TGFβ1 Rabbit Anti-Mouse	1:100	Abcam	ab92486
Chicken anti-Rabbit Alexa 488	1:500	ThermoFisher	A-21441
Goat anti-Rabbit Alexa 647	1:500	ThermoFisher	A-21245

RNA isolation and quantitative real-time PCR (q-PCR)

Cells were lysed with TRIzol Reagent (Ambion) for RNA isolation. Total RNA was isolated from at least 3 independent biological replicates, and RNA quality and quantity measured using the NanoDrop ND100 (Thermo Scientific). Total RNA was reverse-transcribed to cDNA using the High Capacity cDNA Reverse Transcription Kit (Applied Biosystems). qPCR analysis was performed using Sybr Green probes in the AB7900 FAST 384 Detection System (Applied Biosystems), according to the manufacturer´s instructions. Gene expression values were normalized to the housekeeping genes *36b4* and *Cyclophilin*, and expressed as relative mRNA level. Data were analyzed by qBASE program (Biogazelle) obtaining the Ct of the amplification products.

List of primer sequences used for qPCR assays

Gene	Sequence Forward Primer	Sequence Reverse Primer
36b4	GCGACCTGGAAGTCCAACTA	ATCTGCTGCATCTGCTTGG
Cyclophilin	ACAGGTCCTGGCATCTTGTC	CATGGCTTCCACAATGTTCA

Mmp14	CCCTTTTACCAGTGGATGGA	TGTCAAAGTTCCCGTCACAG
Mmp2	GTCGCCCCTAAAACAGACAA	GGTCTCGATGGTGTTCTGGT
Mmp13	ATCCTGGCCACCTTCTTCTT	TTTCTCGGAGCCTGTCAACT
Mmp9	CGTCGTGATCCCCACTTACT	AACACACAGGGTTTGCCTTC
Col1a1	GCTTCAGTGGTTTGGATGGT	AGGGCGACCTCTCTCACC
Pecam	TGCACAGTGATGCTGAACAA	CCATGAGCACAAAGTTCTCG
Kdr	GATCACCATTCATCGCCTCT	CCCAGGAAATTCTGTTTCCA
Col4a2	CAGGATTCCAAGGTGCTCAT	CTGGAAGGCCTCTCATTGAA
Tagln	GATGGAACAGGTGGCTCAAT	AACTGCCCAAAGCCATTAGA
Acta2	GAAAATGAGATGGCCACGGC	TAGGTGGTTTCGTGGATGCC
Pai1	GTAGCACAGGCACTGCAAAA	GCCGAACCACAAAGAGAAAG
Cdh5	CAGGGAATGTGCTTGCCTAT	TCACACGGATGACAGAGGTC
Tie2	CCTTCACCAGGCTGATTGTT	ATAAACCCAGGAGGGAAAT
Cdh2	GCCATCATCGCTATCCTTCT	TTAAAAGCTGCTTGGCTTGG
Col1a2	CCAGCGAAGAACTCATACAGC	GGACACCCCTTCTACGTTGT
Col3a1	CGTAAGCACTGGTGGACAGA	AGCTGCACATCAACGACATC
Zeb2	GAAAAGCAGTTCCCTTCTGC	AGCCTCGAGTGCTCGATAAG
Snai1	TGGAAAGGCCTTCTCTAGGC	CTTCACATCCGAGTGGGTTT

Histology and immunohistochemistry

For histological analysis, hearts were perfused with cold PBS, fixed in 4% PFA overnight and embedded in paraffin. Transverse sections (5 µm) were stained with hematoxylin-eosin (H&E) and Masson trichrome stain according to standard procedures.

For immune-labelling of arterioles, samples were stained with anti-SMA, afterwards with appropriate HRP conjugated antibody, and finally revealed with 3,3'-Diaminobenzidine (DAB) following standard protocols. Whole slide images were acquired with a digital slide scanner (Hamamatsu, Nanozoomer-RS C110730) and then visualized, and exported to TIFF images using NDP.view2 software (Hamamatsu Photonics).

Manual and automated quantifications were performed with Fiji Image J Software (NIH, https://imagej.nih.gov/ij/). The infarct zone (IZ), and the remote zone (RZ) were defined on the basis of H&E-stained sections. In particular, areas containing dying or dead cardiomyocytes (picnotic or absent nuclei, wavy fibers) or fibrotic areas were defined as IZ, whilst the RZ was considered the healthy LV free wall. Measurements were performed on sections obtained from the midpoint of the infarct.

Multi-Photon microscopy and Second Harmonic Generation Imaging

Collagen fibers were visualized in H&E-stained heart sections with a Zeiss LSM 780 microscope coupled to a Spectra-Physics Mai Tai DS [pulse<70 ps] laser, by second harmonic generation (SHG) and multi-photon excitation fluorescence (MPEF) microscopy imaging technique (Abraham et al., 2010). Optical sections were acquired every 3 µm (25x objective) and stitched using Zeiss Zen2 software. The images were then stacked and flattened with Image J software to create maximum intensity Z-projections. Collagen density was calculated using a simple threshold pixel counting method within the IZ and expressed as the area fraction (% SHG). Skewness (asymmetry of pixel distribution) and kurtosis (gray-tone spread-out distribution) were assessed as an indicative of fiber arrangement (Mostaço-Guidolin et al., 2013).

Tissue immunofluorescence and confocal microscopy

Transverse paraffin sections (7 µm) of infarcted hearts were deparaffinized, rehydrated and finally washed in PBS 5 minutes twice. Antigen retrieval was performed by means of pH = 6 citrate buffer for 20 minutes in the microwave at maximum intensity. Afterwards, sections were cooled down at room temperature (RT) for 1 h 30 minutes and then washed with PBS 5 minutes twice. Sections were blocked for 1 h at RT (0.3% Triton X-100, 5% goat serum and 5% BSA in PBS) and primary antibodies were incubated O/N at 4º C (0.3% Triton X-100, 2.5% goat serum and 2.5% BSA in PBS). Next, sections were washed with 0.1% Triton X-100 in PBS at RT for 10 minutes three times and secondary antibodies and DAPI (1/5000) for nuclear staining were then incubated for 1 h 30 minutes at RT (0.3% Triton X-100, 2.5% goat serum and 2.5% BSA in PBS). After four washing steps with 0.1% Triton X-100 in PBS at RT for 10 minutes plus 10 minutes more with PBS alone, slides were mounted with Fluoromont-G (0100-01, Southern Biotech). Images were acquired with a Nikon A1R confocal microscope with sections every 1.5 µm. Three to four areas were acquired within the IZ (the two most distal edges and the center of the infarcted area), and other three to four within the RZ (LV free wall most distal to the infarct).

For the *in vivo* EndMT identification, transverse paraffin thick sections (14 µm) of 7 day-post-infarcted hearts were sequentially stained. For sequential immunostaining, primary rabbit pSMAD2 was incubated O/N at 4ºC (0.3% Triton X-100, 2.5% goat serum and 2.5% BSA in PBS). After washing, goat anti-rabbit Alexa 488 was incubated 1 h at RT (0.3% Triton X-100, 2.5% goat serum and 2.5% BSA in PBS). Sections were afterwards thoroughly washed, and additional blocking was performed with 0.3% Triton X-100, 5% rabbit serum and 5% BSA in PBS 1 h at RT. Directly labelled primary antibodies (mouse anti-SMA-Cy3 and rabbit anti-ERG-647) and DAPI were then incubated 1 hour at RT. Finally, sections were washed and mounted as indicated before. Visual co-localization of the three markers (ERG, SMA, and pSMAD2,) was performed with the orthogonal view plug-in of ImageJ.

For CA-IX quantifications, the total area covered by the CA-IX signal in every image was normalized by the total area, and this ratio was averaged in between individuals. For pSMAD2 quantification in VSMCs and MyoFBs, DAPI nuclei within arteriolar SMA signal were considered VSMCs and DAPI nuclei in non-arteriolar SMA signal were considered MyoFBs. The number of $DAPI^{+}pSMAD2^{+}$ VSMCs and the number of $DAPI^{+}pSMAD2^{+}$ MyoFBs were normalized by the total number of VSMCs or MyoFBs, respectively, and expressed as percentage. Finally, percentages obtained in each region were averaged within individuals. Measurements were performed on sections obtained from the midpoint of the infarct.

List of antibodies used for immunofluorescence assay

Antibody	Concentration	Provider	Reference
Rabbit anti-CAI-IX	1:100	Abcam	ab15086
Goat anti-Rabbit Alexa 546	1:500	ThermoFisher	A-11035
Rat anti-CD31	1:200	Dianova	DIA-310
Goat anti-Rat Alexa 488	1:500	ThermoFisher	A-11006
Rabbit anti-pSMAD2	1:100	Cell Signaling	3108
Goat anti-Rabbit Alexa 647	1:500	ThermoFisher	A-21245
Mouse anti-SMA-Cy3	1:400	Sigma-Aldrich	C6198
Rabbit anti-ERG Alexa 647	1:100	Abcam	ab196149

3D fully automated microvasculature image analysis

Transverse paraffin sections (15 μm) of infarcted hearts were stained with anti-CD31 and anti-SMA antibodies and DAPI for nuclear staining. Two to four images were acquired within the IZ (including the two most distal edges and the center of the IZ) per mouse with a Nikon A1R confocal microscope. Thus, 38 3D images were quantified. Characterization of the microvasculature was performed by means of a fully automated pipeline (Gkontra et al., 2018a). Modules of the pipeline were adapted as previously described (Zak et al., 2019) in order to account for the different animal model (mouse) as well as the use of the relatively thin tissue sections compared to the thick tissue sections of ~100 μm used in the original work. Moreover, since images included both tissue areas and areas belonging to the microscope slide, it was necessary to separate the tissue volume from the background glass area. For this purpose, firstly the images were denoised by means of non-local means filtering (Buades et al., 2005). Subsequently, 3D tissue segmentation was performed by applying Otsu multi-level thresholding technique (Otsu, 1979) on the nuclei channel. It should be noted that the intensity levels used for thresholding varied between three and four depending on the image and they were automatically defined. Voxels of all intensities levels but the lower one were considered

to belong to the tissue. Lastly, holes within the segmented area were automatically identified and filled. It should be noted that apart from normalization purposes, the tissue mask was used to exclude from the corresponding segmentation mask of vessels and SMA^+ cells non-tissue voxels that were incorrectly identified as belonging to vessels or SMA respectively. To this end, element-wise multiplications of the segmentations of vessels and SMA^+ cells with the tissue mask were performed.

Following tissue segmentation, we applied modules of the pipeline that permit the automatic segmentation of nuclei, vessels and SMA^+ cells from the corresponding image channels. Classification of microvessels according to their size and relation with SMA^+ cells into different physiologically meaningful categories was performed as previously described (Zak et al., 2019). Lastly, quantitative parameters regarding the morphology and angioarchitecture of the network as well as the relation of vessels with SMA^+ cells were extracted. The parameters are summarized in Table 3.

Cell culture

Bone marrow-derived macrophages (BMDMs): BMDMs were harvested from 8-10-week-old MT1-$MMP^{f/f}$ and MT1-$MMP^{\Delta LysM}$ mice by flushing femurs and tibias with PBS. Cells were filter through a 100 µm nylon cell strainer (Falcon) and cultured in RPMI (Lonza) supplemented with 20% L929-cell conditioned medium, 10% FBS (Gibco), 1% P/S (Lonza), and 1 mM L-Gln (Lonza) in sterile non-tissue culture treated 10 cm petri dish. BMDMs were activated with 50 ng/ml LPS (Peprotech) O/N to stimulate TGFβ1 production.

Mouse aortic endothelial cells (MAECs): Six to eight aortas from 4-week-old male C57BL/6 mice were pooled to obtain a single-cell suspension (Fogelstrand et al., 2009). Briefly, after carefully aorta dissection and fat removal under a microscope, aortas were incubated in collagenase type I solution (3.33 mg/ml, Worthington) for 5 minutes at 37 ºC. Then, adventitia was removed with forceps, the aortas were then cut into small pieces (1-2 mm) and incubated for 45 minutes at 37 ºC in a type I collagenase (6 mg/ml, Worthington) and elastase (2.5 mg/ml, Worthington) solution DMEM (Lonza) solution. The obtained single cell suspension was plated on 0.5%-gelatin-coated plates in DMEM/F12 supplemented with 20% FBS, 2 mM L-Gln, 1% P/S, and ECGS/H. When culture became confluent, MAECs were positively selected with an antibody against intercellular adhesion molecule 2 (anti-ICAM2; 553325 BD Biosciences) coupled to magnetic beads (Dynabeads™ Sheep Anti-Rat IgG, ThermoFisher), and cultured as indicated in M199 supplemented with 20% FBS, 1% P/S, 2mM L-Gln 1% HEPES, and ECGS/H (Koziol et al., 2012).

Human embryonic kidney 293 (HEK293) cells: HEK293 cells (Lonza) were cultured in DMEM (Lonza) with 10% FBS.

Cardiac Mφs: FACS-sorted Mφs ($CD45^+CD11b^+F4/80^+Ly6C^{low}$ cells) were purified from MT1-$MMP^{f/f}$ and MT1-$MMP^{\Delta LysM}$ hearts on day 7 after MI. They were cultured in DMEM 10% FBS 10 ng/ml M-CSF (Peprotech).

Co-culture and immunofluorescence assay

Mouse aortic ECs (MAECs) were plated at 20,000 per well on 0.5%-gelatin–coated optical p96-well plates in M199 supplemented with 20% FBS, 1% P/S, 2mM L-Gln, 1% HEPES, and ECGS/H, and allowed to attach for 6 h. The medium was then removed and treatments were added in the same medium with reduced serum (5% FBS). The MAEC cultures were overlaid with 30,000 LPS-activated MT1-$MMP^{f/f}$ or MT1-$MMP^{\Delta LysM}$ BMDMs, or with 50,000 cardiac Mφs from 7-day post-MI MT1-$MMP^{f/f}$ or MT1-$MMP^{\Delta LysM}$ mice. Co-cultures were maintained for 4 days. As a positive control for EndMT, MAEC monocultures were treated with 10 ng/ml TGFβ1.

After two washes in HBBS, cultures were fixed for 10 minutes at room temperature (RT) in 4% paraformaldehyde. Cells were then permeabilized for 10 minutes at RT in 0.2% Triton X-100 in phosphate-buffered saline (PBS) and blocked for 1 h at RT in 5% goat serum and 5% BSA in PBS. After overnight incubation with primary antibodies at 4º C in 2.5% goat serum and 2.5% BSA in PBS, cells were washed three times with PBS at RT and then incubated with secondary antibodies and DAPI for 1 h 30 minutes at RT in 2.5% goat serum and 2.5% BSA in PBS. Cells were then washed four times with PBS. Cells were visualized under a Nikon A1R microscope, and images were acquired as 2x2 tile scans of 5x1 µm sections. Maximal projections were used for quantifications.

Co-cultures and qPCR assay

MAECs were plated at 150,000 per well on 0.5%-gelatin–coated optical p6-well plates in M199 supplemented with 20% FBS, 1% P/S, 2mM L-Gln, 1% HEPES, and ECGS/H, and allowed to attach for 6 h. The medium was then removed and treatments were added in the same medium with reduced serum (5% FBS). The MAEC cultures were overlaid with 250,000 LPS-activated MT1-$MMP^{f/f}$ or MT1-$MMP^{\Delta LysM}$ BMDMs. Co-cultures were maintained for 4 days. As a positive control for EndMT, MAEC monocultures were treated with 10 ng/ml TGFβ1. Afterwards, cells were lysed with TRIzol Reagent (Ambion) for RNA isolation following manufacturer's instructions.

HEK293 transfection and luciferase assay

HEK293 cells (40%-50% confluence) were transfected over 6 h with the plasmid p3TP-lux (Wrana et al., 1992) with 2.5M $CaCl_2$ in HEPES Buffered Saline (HBS). This plasmid

contains luciferase downstream of the PAI-1 promoter, therefore the luciferase activity is proportional to the production of bioactive TGFβ1 (Abe et al., 1994).

Luciferase assay was carried out as described (Abe et al., 1994). In brief, transfected HEK293 cells were plated at a density of 30,000 cells per well in p96-well plates and allowed to adhere for 6 h. Then, 10 ng/mL of recombinant TGFβ1 (Peprotech) for the positive control, 40,000 MT1-MMP$^{f/f}$ BMDMs or 40,000 MT1-MMP$^{\Delta LysM}$ BMDMs (previously activated with 50 ng/ml LPS O/N) were added to the plate. After 24 h of incubation, cells were lysed with Passive Lysis Buffer (Promega), and luciferase activity was assayed with the Promega Luciferase Assay according to manufacturer's instructions.

When the assay was carried out with cardiac Mφs, CD45^{+}CD11b^{+}F4/80^{+}Ly6C^{low} cells were sorted as indicated in Figure S1A-B from 7 days post-MI MT1-MMP$^{f/f}$ or MT1-MMP$^{\Delta LysM}$ hearts. 50,000 cardiac Mφs were added to the previously transfected and plated HEKs (as indicated above), and M-CSF (10 ng/ml) was kept in the medium for the 24 h of culture to maintain cardiac Mφs alive. Then, cells were lysed with Passive Lysis Buffer (Promega), and luciferase activity was assayed with the Promega Luciferase Assay according to manufacturer's instructions.

Lentiviral transduction

The full-length MT1-MMP sequence (FL) or mutated version to disable catalytic activity (E240A) were cloned into the SFFV-IRESGFP lentiviral backbone. Lentiviruses expressing Mock, MT1-MMP FL, or MT1-MMP E240A were prepared and titered as previously described (Esteban et al., 2019). For viral inoculation, we incubated MT1-MMP$^{\Delta LysM}$ BMDMs with the viral supernatants (MOI = 10) in RPMI supplemented with 20% L929-cell conditioned medium, 10% FBS, 1% P/S, and 1mM L-Gln for 48 h. GFP signal was detected by fluorescent microscopy in transduced BMDMs. We then removed the viral supernatants and stimulated the cells with 50 ng/ml LPS O/N. Afterwards, the media was removed and cells were cultured in DMEM 10% FBS for 24 h to obtain conditioned media. Conditioned media was then added to HEK293 cells for luciferase assay as described above.

Cell extract preparation and Western blot analysis

MT1-MMP$^{f/f}$ or MT1-MMP$^{\Delta LysM}$ BMDMs were treated with 1 ng/mL LPS (Peprotech) for 24 h to stimulate TGFβ1 production. Prior to lysate collection, cell viability was determined by microscopy under bright field and cell debris removed by 2 washes of monolayers with PBS. For preparation of total lysates, 4x10^{6} BMDMs were incubated in RIPA buffer, containing 50 mM Tris-HCl, pH 8; 150 mM NaCl; 1% Triton X-100; 0.5% sodium deoxycholate; 0.1% SDS; 1mM PMSF (Sigma) and a protease and phosphatase inhibitor cocktail (Sigma), for 30 minutes at 4º C in the rotor. The lysate was centrifuged (14,000 g, 10 minutes), and the

supernatant containing the proteins was transferred to a new tube. For subcellular fractioning, $4x10^6$ BMDMs were incubated in HES buffer, containing 20mM HEPES, 1mM EDTA, 250mM sucrose and a protease and phosphatase inhibitor cocktail (Sigma), for 10 minutes at 4º C. Cells were lysed through a 22G needle followed by a 25G needle, and centrifuged at 500 g for 8 minutes to pellet the unbroken cells. Then, the supernatant was transferred to an empty tube and centrifuged at 10,000 g for 12 minutes to separate the cytosolic (supernatant) and the membrane (pellet) protein fractions.

Protein concentration was estimated using Bradford Assay (Bio-Rad) and 30 µg of total protein were separated by 10% SDS-PAGE and transferred to a nitrocellulose membrane (Bio-Rad). Correct protein loading was confirmed by Ponceau staining. Membranes were incubated O/N with antibodies against TGFβ1 (Santa Cruz, sc-146), TfR (Abcam; ab84036), and α-tubulin (Sigma; T6074) at 1:500 (for TGFβ1) or 1:1000 dilutions (for TfR and α-tubulin), and then thoroughly washed and incubated with HRP-conjugated anti-rabbit (Jackson 111-035-003) or anti-mouse (Jackson 115-035-003) antibodies (1:7500). Blots were visualized using the chemiluminescent Immobilon Classico Western HRP substrate (Millipore). Chemiluminiscent signal was detected using ImageQuant™ LAS 4000 and densitometry analysis performed using ImageJ. The ratio between proteins of interest (TGFβ1) and endogenous control (TfR) was calculated for data normalization. Graphs represent fold change calculated based on normalized data.

Statistics

Data are presented as mean ± SEM. Unpaired *t*-test was used when two groups were compared, and comparison of more than two datasets was done using one-way analysis of variance (ANOVA) with Tukey's post-test. Comparisons of two-time curves were performed using two-way ANOVA followed by Tukey's post-test. All statistical analyses were performed using Prism v7 (GraphPad Software, California, USA). Differences were considered significant when $p < 0.05$, and represented as * $p < 0.05$, ** $p < 0.01$, *** $p < 0.001$, and **** $p < 0.0001$.

ACKNOWLEDGMENTS

We thank Ángel Colmenar and the CNIC Cellomics, Proteomics, Microscopy, Advanced Imaging, and Animal Units for technical support and Simon Bartlett for English editing. We also thank the Proteomics Unit at the Vall d'Hebron Institute of Oncology. We thank Carlos López-Otín (Universidad de Oviedo) for providing the MT1-MMP1$^{f/f}$ mice, Ralf Adams (Max Planck Institute of Molecular Biomedicine) for providing the Cdh5-Cre^{ERT2} mice, and Carmelo Bernabeu (Centro de Investigaciones Biológicas, CIB-CSIC) for the p3TP-lux plasmid. This study was supported by grants from the Spanish Ministry of Science, Innovation and Universities (SAF2017-90604-REDT-NurCaMein, RTI2018-095928-BI00 to M.R.;

SAF2017-83229-R to A.G.A.), Comunidad de Madrid (MOIR-B2017/BMD-3684) to M.R, and La Marató de TV3 Foundation to D.G.D, A.G.A., and M.R.. L.A.H. is funded by a fellowship from La Caixa-CNIC. A.S.E. is funded by a fellowship from La Caixa and supported by La Residencia de Estudiantes. The CNIC is supported by the MCNU and the Pro CNIC Foundation and is a Severo Ochoa Center of Excellence (SEV-2015-0505).

COMPETING INTERESTS

The authors declare no competing interests.

REFERENCES

Abe, M., Harpel, J.G., Metz, C.N., Nunes, I., Loskutoff, D.J., and Rifkin, D.B. (1994). An assay for transforming growth factor-beta using cells transfected with a plasminogen activator inhibitor-1 promoter-luciferase construct. Anal Biochem *216*, 276-284.

Abraham, T., Carthy, J., and McManus, B. (2010). Collagen matrix remodeling in 3-dimensional cellular space resolved using second harmonic generation and multiphoton excitation fluorescence. Journal of structural biology *169*, 36-44.

Abram, C.L., Roberge, G.L., Hu, Y., and Lowell, C.A. (2014). Comparative analysis of the efficiency and specificity of myeloid-Cre deleting strains using ROSA-EYFP reporter mice. J Immunol Methods *408*, 89-100.

Aisagbonhi, O., Rai, M., Ryzhov, S., Atria, N., Feoktistov, I., and Hatzopoulos, A.K. (2011). Experimental myocardial infarction triggers canonical Wnt signaling and endothelial-to-mesenchymal transition. Dis Model Mech *4*, 469-483.

Alonso-Herranz, L., Porcuna, J., and Ricote, M. (2019). Isolation and Purification of Tissue Resident Macrophages for the Analysis of Nuclear Receptor Activity. Methods in molecular biology (Clifton, NJ) *1951*, 59-73.

Arnold, T.D., Niaudet, C., Pang, M.F., Siegenthaler, J., Gaengel, K., Jung, B., Ferrero, G.M., Mukouyama, Y.S., Fuxe, J., Akhurst, R.*, et al.* (2014). Excessive vascular sprouting underlies cerebral hemorrhage in mice lacking alphaVbeta8-TGFbeta signaling in the brain. Development *141*, 4489-4499.

Bajpai, G., Bredemeyer, A., Li, W., Zaitsev, K., Koenig, A.L., Lokshina, I., Mohan, J., Ivey, B., Hsiao, H.M., Weinheimer, C.*, et al.* (2019). Tissue Resident CCR2- and CCR2+ Cardiac Macrophages Differentially Orchestrate Monocyte Recruitment and Fate Specification Following Myocardial Injury. Circulation research *124*, 263-278.

Benjamin, E.J., Blaha, M.J., Chiuve, S.E., Cushman, M., Das, S.R., Deo, R., de Ferranti, S.D., Floyd, J., Fornage, M., Gillespie, C.*, et al.* (2017). Heart Disease and Stroke Statistics-2017 Update: A Report From the American Heart Association. Circulation *135*, e146-e603.

Buades, A., Coll, B., and Morel, J.-M. (2005). A Non-Local Algorithm for Image Denoising. In Proceedings of the 2005 IEEE Computer Society Conference on Computer Vision and Pattern Recognition (CVPR'05) - Volume 2 - Volume 02 (IEEE Computer Society), pp. 60-65.

Clausen, B.E., Burkhardt, C., Reith, W., Renkawitz, R., and Forster, I. (1999). Conditional gene targeting in macrophages and granulocytes using LysMcre mice. Transgenic research *8*, 265-277.

Creemers, E.E., Cleutjens, J.P., Smits, J.F., and Daemen, M.J. (2001). Matrix metalloproteinase inhibition after myocardial infarction: a new approach to prevent heart failure? Circulation research *89*, 201-210.

Cruz-Adalia, A., Jimenez-Borreguero, L.J., Ramirez-Huesca, M., Chico-Calero, I., Barreiro, O., Lopez-Conesa, E., Fresno, M., Sanchez-Madrid, F., and Martin, P. (2010). CD69 limits the severity of cardiomyopathy after autoimmune myocarditis. Circulation *122*, 1396-1404.

Daseke, M.J., 2nd, Valerio, F.M., Kalusche, W.J., Ma, Y., DeLeon-Pennell, K.Y., and Lindsey, M.L. (2019). Neutrophil proteome shifts over the myocardial infarction time continuum. Basic Res Cardiol *114*, 37.

Dick, S.A., Macklin, J.A., Nejat, S., Momen, A., Clemente-Casares, X., Althagafi, M.G., Chen, J., Kantores, C., Hosseinzadeh, S., Aronoff, L.*, et al.* (2019). Self-renewing resident cardiac macrophages limit adverse remodeling following myocardial infarction. Nat Immunol *20*, 29-39.

Esteban, S., Clemente, C., Koziol, A., Gonzalo, P., Rius, C., Martinez, F., Linares, P.M., Chaparro, M., Urzainqui, A., Andres, V.*, et al.* (2019). Endothelial MT1-MMP targeting limits intussusceptive angiogenesis and colitis via TSP1/nitric oxide axis. EMBO molecular medicine, e10862.

Evrard, S.M., Lecce, L., Michelis, K.C., Nomura-Kitabayashi, A., Pandey, G., Purushothaman, K.R., d'Escamard, V., Li, J.R., Hadri, L., Fujitani, K.*, et al.* (2016). Endothelial to mesenchymal transition is common in atherosclerotic lesions and is associated with plaque instability. Nat Commun *7*, 11853.

Fogelstrand, P., Feral, C.C., Zargham, R., and Ginsberg, M.H. (2009). Dependence of proliferative vascular smooth muscle cells on CD98hc (4F2hc, SLC3A2). J Exp Med *206*, 2397-2406.

Frangogiannis, N.G. (2015). Pathophysiology of Myocardial Infarction. Compr Physiol *5*, 1841-1875.

Frangogiannis, N.G. (2020). Transforming growth factor–β in tissue fibrosis Journal of Experimental Medicine *217*, 16.

759 Gallego-Colon, E., Villalba, M., Tonkin, J., Cruz, F., Bernal, J.A., Jimenez-Borregureo, L.J.,
760 Schneider, M.D., Lara-Pezzi, E., and Rosenthal, N. (2016). Intravenous delivery of adeno-
761 associated virus 9-encoded IGF-1Ea propeptide improves post-infarct cardiac remodelling.
762 NPJ Regenerative medicine *1*, 16001.

763 Garmon, T., Wittling, M., and Nie, S. (2018). MMP14 Regulates Cranial Neural Crest
764 Epithelial-to-Mesenchymal Transition and Migration. Dev Dyn *247*, 1083-1092.

765 Gkontra, P., Norton, K.A., Zak, M.M., Clemente, C., Aguero, J., Ibanez, B., Santos, A., Popel,
766 A.S., and Arroyo, A.G. (2018a). Deciphering microvascular changes after myocardial
767 infarction through 3D fully automated image analysis. Sci Rep *8*, 1854.

768 Gkontra, P., Norton, K.A., Zak, M.M., Clemente, C., Aguero, J., Ibanez, B., Santos, A., Popel,
769 A.S., and Arroyo, A.G. (2018b). Deciphering microvascular changes after myocardial
770 infarction through 3D fully automated image analysis. Scientific reports *8*, 018-19758.

771 Gutierrez-Fernandez, A., Soria-Valles, C., Osorio, F.G., Gutierrez-Abril, J., Garabaya, C.,
772 Aguirre, A., Fueyo, A., Fernandez-Garcia, M.S., Puente, X.S., and Lopez-Otin, C. (2015). Loss
773 of MT1-MMP causes cell senescence and nuclear defects which can be reversed by retinoic
774 acid. Embo J *34*, 1875-1888.

775 Helmke, A., Casper, J., Nordlohne, J., David, S., Haller, H., Zeisberg, E.M., and von
776 Vietinghoff, S. (2019). Endothelial-to-mesenchymal transition shapes the atherosclerotic
777 plaque and modulates macrophage function. Faseb j *33*, 2278-2289.

778 Henderson, N.C., Arnold, T.D., Katamura, Y., Giacomini, M.M., Rodriguez, J.D., McCarty,
779 J.H., Pellicoro, A., Raschperger, E., Betsholtz, C., Ruminski, P.G.*, et al.* (2013). Targeting of
780 alphav integrin identifies a core molecular pathway that regulates fibrosis in several organs.
781 Nature medicine *19*, 1617-1624.

782 Hofmann, J.J., Briot, A., Enciso, J., Zovein, A.C., Ren, S., Zhang, Z.W., Radtke, F., Simons,
783 M., Wang, Y., and Iruela-Arispe, M.L. (2012). Endothelial deletion of murine Jag1
784 leads to valve calcification and congenital heart defects associated with Alagille syndrome.
785 Development *139*, 4449-4460.

786 Hudson, M.P., Armstrong, P.W., Ruzyllo, W., Brum, J., Cusmano, L., Krzeski, P., Lyon, R.,
787 Quinones, M., Theroux, P., Sydlowski, D.*, et al.* (2006). Effects of selective matrix
788 metalloproteinase inhibitor (PG-116800) to prevent ventricular remodeling after myocardial
789 infarction: results of the PREMIER (Prevention of Myocardial Infarction Early Remodeling)
790 trial. J Am Coll Cardiol *48*, 15-20.

791 Imaizumi, N., Monnier, Y., Hegi, M., Mirimanoff, R.O., and Ruegg, C. (2010). Radiotherapy
792 suppresses angiogenesis in mice through TGF-betaRI/ALK5-dependent inhibition of
793 endothelial cell sprouting. PLoS One *5*, e11084.

794 Inserte, J., Aluja, D., Barba, I., Ruiz-Meana, M., Miro, E., Poncelas, M., Vilardosa, U.,
795 Castellano, J., and Garcia-Dorado, D. (2019). High-fat diet improves tolerance to myocardial
796 ischemia by delaying normalization of intracellular PH at reperfusion. J Mol Cell Cardiol *133*,
797 164-173.

798 Kanisicak, O., Khalil, H., Ivey, M.J., Karch, J., Maliken, B.D., Correll, R.N., Brody, M.J., SC,
799 J.L., Aronow, B.J., Tallquist, M.D*., et al.* (2016). Genetic lineage tracing defines myofibroblast
800 origin and function in the injured heart. Nat Commun *7*, 12260.

801 Koenig, G.C., Rowe, R.G., Day, S.M., Sabeh, F., Atkinson, J.J., Cooke, K.R., and Weiss, S.J.
802 (2012). MT1-MMP-dependent remodeling of cardiac extracellular matrix structure and function
803 following myocardial infarction. The American journal of pathology *180*, 1863-1878.

804 Kolk, M.V., Meyberg, D., Deuse, T., Tang-Quan, K.R., Robbins, R.C., Reichenspurner, H.,
805 and Schrepfer, S. (2009). LAD-ligation: a murine model of myocardial infarction. Journal of
806 visualized experiments : JoVE.

807 Kovacic, J.C., Dimmeler, S., Harvey, R.P., Finkel, T., Aikawa, E., Krenning, G., and Baker,
808 A.H. (2019). Endothelial to Mesenchymal Transition in Cardiovascular Disease: JACC State-
809 of-the-Art Review. J Am Coll Cardiol *73*, 190-209.

810 Koziol, A., Gonzalo, P., Mota, A., Pollan, A., Lorenzo, C., Colome, N., Montaner, D., Dopazo,
811 J., Arribas, J., Canals, F*., et al.* (2012). The protease MT1-MMP drives a combinatorial
812 proteolytic program in activated endothelial cells. Faseb j *26*, 4481-4494.

813 Krishnamurthy, P., Rajasingh, J., Lambers, E., Qin, G., Losordo, D.W., and Kishore, R. (2009).
814 IL-10 inhibits inflammation and attenuates left ventricular remodeling after myocardial
815 infarction via activation of STAT3 and suppression of HuR. Circulation research *104*, e9-18.

816 Lawrence, D.A. (2001). Latent-TGF-beta: an overview. Mol Cell Biochem *219*, 163-170.

817 Li, Y., Lui, K.O., and Zhou, B. (2018). Reassessing endothelial-to-mesenchymal transition in
818 cardiovascular diseases. Nat Rev Cardiol *15*, 445-456.

819 Madisen, L., Zwingman, T.A., Sunkin, S.M., Oh, S.W., Zariwala, H.A., Gu, H., Ng, L.L.,
820 Palmiter, R.D., Hawrylycz, M.J., Jones, A.R*., et al.* (2010). A robust and high-throughput Cre
821 reporting and characterization system for the whole mouse brain. Nat Neurosci *13*, 133-140.

822 Maecker, H.T., Frey, T., Nomura, L.E., and Trotter, J. (2004). Selecting fluorochrome
823 conjugates for maximum sensitivity. Cytometry Part A *62*, 169-173.

824 Moore-Morris, T., Guimaraes-Camboa, N., Banerjee, I., Zambon, A.C., Kisseleva, T.,
825 Velayoudon, A., Stallcup, W.B., Gu, Y., Dalton, N.D., Cedenilla, M*., et al.* (2014). Resident
826 fibroblast lineages mediate pressure overload-induced cardiac fibrosis. The Journal of clinical
827 investigation *124*, 2921-2934.

828 Mostaço-Guidolin, L.B., Ko, A.C.T., Wang, F., Xiang, B., Hewko, M., Tian, G., Major, A.,
829 Shiomi, M., and Sowa, M.G. (2013). Collagen morphology and texture analysis: from statistics
830 to classification. *3*, 2190.

831 Mu, D., Cambier, S., Fjellbirkeland, L., Baron, J.L., Munger, J.S., Kawakatsu, H., Sheppard,
832 D., Broaddus, V.C., and Nishimura, S.L. (2002). The integrin alpha(v)beta8 mediates epithelial
833 homeostasis through MT1-MMP-dependent activation of TGF-beta1. J Cell Biol *157*, 493-507.

834 Nahrendorf, M., Swirski, F.K., Aikawa, E., Stangenberg, L., Wurdinger, T., Figueiredo, J.L.,
835 Libby, P., Weissleder, R., and Pittet, M.J. (2007). The healing myocardium sequentially
836 mobilizes two monocyte subsets with divergent and complementary functions. J Exp Med *204*,
837 3037-3047.

838 Nguyen, H.L., Kadam, P., Helkin, A., Cao, K., Wu, S., Samara, G.J., Zhang, Q., Zucker, S.,
839 and Cao, J. (2016). MT1-MMP Activation of TGF-beta Signaling Enables Intercellular
840 Activation of an Epithelial-mesenchymal Transition Program in Cancer. Curr Cancer Drug
841 Targets *16*, 618-630.

842 O'Rourke, S.A., Dunne, A., and Monaghan, M.G. (2019). The Role of Macrophages in the
843 Infarcted Myocardium: Orchestrators of ECM Remodeling. Front Cardiovasc Med *6*, 101.

844 Ohuchi, E., Imai, K., Fujii, Y., Sato, H., Seiki, M., and Okada, Y. (1997). Membrane type 1
845 matrix metalloproteinase digests interstitial collagens and other extracellular matrix
846 macromolecules. The Journal of biological chemistry *272*, 2446-2451.

847 Otsu, N. (1979). A Threshold Selection Method from Gray-Level Histograms. IEEE
848 Transactions on Systems, Man and Cybernetics *9*, 62-66.

849 Page-McCaw, A., Ewald, A.J., and Werb, Z. (2007). Matrix metalloproteinases and the
850 regulation of tissue remodelling. Nat Rev Mol Cell Biol *8*, 221-233.

851 Panizzi, P., Swirski, F.K., Figueiredo, J.L., Waterman, P., Sosnovik, D.E., Aikawa, E., Libby,
852 P., Pittet, M., Weissleder, R., and Nahrendorf, M. (2010). Impaired infarct healing in
853 atherosclerotic mice with Ly-6C(hi) monocytosis. J Am Coll Cardiol *55*, 1629-1638.

854 Piera-Velazquez, S., and Jimenez, S.A. (2019). Endothelial to Mesenchymal Transition: Role
855 in Physiology and in the Pathogenesis of Human Diseases. Physiol Rev *99*, 1281-1324.

856 Pinto, A.R., Ilinykh, A., Ivey, M.J., Kuwabara, J.T., D'Antoni, M.L., Debuque, R., Chandran, A.,
857 Wang, L., Arora, K., Rosenthal, N.A.*, et al.* (2016). Revisiting Cardiac Cellular Composition.
858 Circulation research *118*, 400-409.

859 Ram, R., Mickelsen, D.M., Theodoropoulos, C., and Blaxall, B.C. (2011). New approaches in
860 small animal echocardiography: imaging the sounds of silence. American journal of physiology
861 Heart and circulatory physiology *301*, H1765-1780.

Sato, H., Takino, T., Okada, Y., Cao, J., Shinagawa, A., Yamamoto, E., and Seiki, M. (1994). A matrix metalloproteinase expressed on the surface of invasive tumour cells. Nature *370*, 61-65.

Spinale, F.G., Mukherjee, R., Zavadzkas, J.A., Koval, C.N., Bouges, S., Stroud, R.E., Dobrucki, L.W., and Sinusas, A.J. (2010). Cardiac restricted overexpression of membrane type-1 matrix metalloproteinase causes adverse myocardial remodeling following myocardial infarction. The Journal of biological chemistry *285*, 30316-30327.

Swirski, F.K., Nahrendorf, M., Etzrodt, M., Wildgruber, M., Cortez-Retamozo, V., Panizzi, P., Figueiredo, J.L., Kohler, R.H., Chudnovskiy, A., Waterman, P.*, et al.* (2009). Identification of splenic reservoir monocytes and their deployment to inflammatory sites. Science *325*, 612-616.

Talmi-Frank, D., Altboum, Z., Solomonov, I., Udi, Y., Jaitin, D.A., Klepfish, M., David, E., Zhuravlev, A., Keren-Shaul, H., Winter, D.R.*, et al.* (2016). Extracellular Matrix Proteolysis by MT1-MMP Contributes to Influenza-Related Tissue Damage and Mortality. Cell Host Microbe *20*, 458-470.

van Amerongen, M.J., Harmsen, M.C., van Rooijen, N., Petersen, A.H., and van Luyn, M.J. (2007). Macrophage depletion impairs wound healing and increases left ventricular remodeling after myocardial injury in mice. The American journal of pathology *170*, 818-829.

Walter, W., Alonso-Herranz, L., Trappetti, V., Crespo, I., Ibberson, M., Cedenilla, M., Karaszewska, A., Nunez, V., Xenarios, I., Arroyo, A.G.*, et al.* (2018). Deciphering the Dynamic Transcriptional and Post-transcriptional Networks of Macrophages in the Healthy Heart and after Myocardial Injury. Cell reports *23*, 622-636.

Wang, Y., Nakayama, M., Pitulescu, M.E., Schmidt, T.S., Bochenek, M.L., Sakakibara, A., Adams, S., Davy, A., Deutsch, U., Luthi, U.*, et al.* (2010). Ephrin-B2 controls VEGF-induced angiogenesis and lymphangiogenesis. Nature *465*, 483-486.

Wrana, J.L., Attisano, L., Carcamo, J., Zentella, A., Doody, J., Laiho, M., Wang, X.F., and Massague, J. (1992). TGF beta signals through a heteromeric protein kinase receptor complex. Cell *71*, 1003-1014.

Xia, Y., Lee, K., Li, N., Corbett, D., Mendoza, L., and Frangogiannis, N.G. (2009). Characterization of the inflammatory and fibrotic response in a mouse model of cardiac pressure overload. Histochem Cell Biol *131*, 471-481.

Xiong, Y., Zhang, J., Shi, L., Ning, Y., Zhu, Y., Chen, S., Yang, M., Chen, J., Zhou, G.W., and Li, Q. (2017). NOGO-B promotes EMT in lung fibrosis via MMP14 mediates free TGF-beta1 formation. Oncotarget *8*, 71024-71037.

Xu, X., Friehs, I., Hu, T.Z., Melnychenko, I., Tampe, B., Alnour, F., Iascone, M., Kalluri, R., Zeisberg, M., Nido, P.J.d., *et al.* (2015). Endocardial Fibroelastosis Is Caused by Aberrant Endothelial to Mesenchymal Transition. Circulation research *116*, 857-866.

Yabluchanskiy, A., Li, Y., Chilton, R.J., and Lindsey, M.L. (2013). Matrix metalloproteinases: drug targets for myocardial infarction. Current drug targets *14*, 276-286.

Zak, M.M., Gkontra, P., Clemente, C., Squadrito, M.L., Ferrarini, A., Mota, R.A., Oliver, E., Rocha, S., Aguero, J., Vazquez, J., *et al.* (2019). Sequential Bone-Marrow Cell Delivery of VEGFA/S1P Improves Vascularization and Limits Adverse Cardiac Remodeling After Myocardial Infarction in Mice. Hum Gene Ther.

Zavadzkas, J.A., Mukherjee, R., Rivers, W.T., Patel, R.K., Meyer, E.C., Black, L.E., McKinney, R.A., Oelsen, J.M., Stroud, R.E., and Spinale, F.G. (2011). Direct regulation of membrane type 1 matrix metalloproteinase following myocardial infarction causes changes in survival, cardiac function, and remodeling. American journal of physiology Heart and circulatory physiology *301*, H1656-1666.

Zeisberg, E.M., Tarnavski, O., Zeisberg, M., Dorfman, A.L., McMullen, J.R., Gustafsson, E., Chandraker, A., Yuan, X., Pu, W.T., Roberts, A.B., *et al.* (2007). Endothelial-to-mesenchymal transition contributes to cardiac fibrosis. Nature medicine *13*, 952-961.

Zhang, Z., Wang, J.A., Xu, Y., Jiang, Z., Wu, R., Wang, L., Chen, P., Hu, X., and Yu, H. (2013). Menstrual blood derived mesenchymal cells ameliorate cardiac fibrosis via inhibition of endothelial to mesenchymal transition in myocardial infarction. Int J Cardiol *168*, 1711-1714.

TABLES

	MT1-MMP$^{f/f}$	MT1-MMP$^{\Delta LysM}$
BW (g)	18.62 ± 2.00	19.53 ± 2.25
HW/BW (mg/g)	4.91 ± 0.28	4.94 ± 0.19
HR (beats/min)	462 ± 14	463 ± 17
PR (ms)	39.82 ± 1.18	37.70 ± 1.21
QRS (ms)	25.41 ± 1.06	26.18 ± 0.88
LVEF (%)	53.52 ± 1.72	53.14 ± 2.31
LVVols (µL)	21.53 ± 1.36	19.98 ± 1.60
LVVold (µL)	25.26 ± 0.96	22.22 ± 0.90
FS (%)	26.58 ± 0.89	26.33 ± 1.51
LVIDs (mm)	3.67 ± 0.06	3.54 ± 0.08
LVIDd (mm)	2.7 ± 0.06	2.62 ± 0.10

Table 1. Mφ MT1-MMP deletion does not affect homeostatic cardiac function. Echocardiography and electrocardiography comparisons between 10-week-old MT1-MMP$^{f/f}$ and MT1-MMP$^{\Delta LysM}$ mice. Data are means ± SEM of 10 mice per group. Unpaired *t*-test. BW, body weight; FS, fraction shortening; HR, heart rate; HW, heart weight; LVEF, LV ejection fraction; LVIDd, LV end-diastolic internal diameter; LVIDs, LV end-systolic internal diameter; LVVold, LV end-diastolic volumen; LVVols, LV end-systolic volume.

	MT1-MMP$^{f/f}$		MT1-MMP$^{\Delta LysM}$	
	%	cells (x10^3)/ml	%	cells (x10^3)/ml
Neutrophils	9.50 ± 0.98	0.74 ± 0.11	11.01 ± 1.43	0.88 ± 0.13
Lymphocytes	86.75 ± 1.29	6.97 ± 1.00	84.79 ± 1.68	6.84 ± 0.54
Monocytes	0.89 ± 0.14	0.08 ± 0.02	1.20 ± 0.13	0.10 ± 0.01
Eosinophils	2.45 ± 0.44	0.21 ± 0.06	2.48 ± 0.51	0.20 ± 0.04
Basophils	0.41 ± 0.08	0.03 ± 0.01	0.53 ± 0.09	0.05 ± 0.01

926 **Table 2. Mφ MT1-MMP deletion does not affect circulating bone-marrow derived**
927 **populations.** Hematograms from 10-week-old MT1-MMP$^{f/f}$ and MT1-MMP$^{\Delta LysM}$ mice. Data are
928 means ± SEM of 8 mice per group.

929

Minkowski-Based Metrics	**MT1-MMP$^{f/f}$**	**MT1-MMP$^{\Delta LysM}$**
Vascular Volume Density (%)	12.65 ± 0.36	13.26 ± 0.34 *
Vascular Surface Area Density (x 10^{-3}) ($\mu m^2/\mu m^3$)	21.24 ± 2.5	23.13 ± 1.92
Graph-Based Metrics		
Vascular Segment length (µm)	6.97 ± 0.74	6.2 ± 0.18
Vascular Segment surface (μm^2)	36.41 ± 5.52	29.5 ± 1.6
Vascular Segment volume (μm^3)	17 ± 3.8	12.54 ± 1.53
Tortuosity (µm/µm)	1.61 ± 0.02	1.61 ± 0.03
Vascular Segments (x 10^5)[a]	4.12 ± 0.68	5.48 ± 0.53
Vascular Segments[b]	144.17 ± 14.15	158.27 ± 2.31
Vessels of diameter <= 3 (µm) (%)	95.48 ± 2.55	96.97 ± 1.85 *
Vessels of diameter between 3 and 6 (µm) (%)	4.51 ± 2.52	3.03 ± 1.85
Vessels of diameter > 6 (µm) (%)	0.012 ± 0.001	0.028 ± 0.001
Vessels of diameter <= 3 (µm) (x 10^5)[a]	3.97 ± 0.71	5.33 ± 0.59 *
Vessels of diameter between 3 and 6 (µm) (x 10^5)[a]	0.16 ± 0.06	0.15 ± 0.09
Vessels of diameter > 6 (µm)[a]	32.81 ± 0.0001	73.36 ± 0.0001
Branching Nodes (x 10^4)[a]	22.39 ± 4.28	30.43 ± 2.51
Blind-ends/sprouts (x 10^4)[a]	6.06 ± 0.92	7.93 ± 1.2
Branching nodes[b]	77.38 ± 9.59	87.31 ± 2.14
Blind-ends/sprouts[b]	24.09 ± 4.07	25.9 ± 1.66
SMA-related metrics		
Vessels covered with SMA (%)	47.2 ± 17.67	53.54 ± 12
SMA^+ layer thikness (µm)	2.98 ± 0.76	2.72 ± 0.43
Damage index	0.21 ± 0.11	0.19 ± 0.09
Myofibroblasts (x 10^4)[a]	2.51 ± 1.18	2.05 ± 0.64
Myofibroblasts[b]	8.9 ± 3.8	5.97 ± 1.47
Myofibroblasts (x 10^5)[d]	19.1 ± 10	15.3 ± 4.7

SMA+ perivascular cells (x 10^4)[a]	4.74 ± 2.36	5.25 ± 1.59
SMA+ perivascular cells[b]	16.16 ± 7.31	15.48 ± 3.65
SMA+ perivascular cells (x 10^5)[d]	36.3 ± 19.3	38.9 ± 10.8
Efficiency in oxygen diffusion		
Maximal Extravascualr Distance (µm)	51.47 ± 10.83	45.47 ± 7.11
Median Extravascualr Distance (µm)	14.28 ± 2.64	13 ± 1.38
Capillary Density[c]	1201 ± 298.12	1720 ± 368.61 *
Intercapillary Distance	8.09 ± 0.51	7.31 ± 0.27 *
Diffusion Distance	10.84 ± 0.51	9.76 ± 0.49 *
Additional cell-related metrics		
Endothelial cells (x 10^4)[a]	6.2 ± 1.05	7.91 ± 1.21
Endothelial cells[b]	22.45 ± 3.91	23.16 ± 1.34
Endothelial cells (x 10^5)[d]	46.6 ± 8.1	58.8 ± 7.7 *

Table 3. Quantitative analysis of microvasculature parameters in infarcted cardiac tissue from MT1-MMP$^{f/f}$ and MT1-MMP$^{\Delta LysM}$ mice on day 7 after MI. Capillaries correspond to CD31$^+$SMA$^-$ vessels of diameter < 3 µm. Data are means ± SEM of 5-6 mice per genotype. Unpaired *t*-test. Significant differences are indicated as * $p < 0.05$. [a] per mm^3 of tissue, [b] per mm vessel length, [c] per mm^2 of tissue, [d] per mm^3 vessel volume.

FIGURES AND FIGURE LEGENDS

Figure 1. Mφ-restricted MT1-MMP deficiency attenuates LV dysfunction and dilation and reduces collagen deposition after MI. (A) mRNA expression levels of genes related to ECM-remodeling assessed by qPCR in sorted Mφs at the indicated post-MI stages. Data are means ± SEM of 3 independent pools of 3-5 mice per time point. One-way ANOVA followed by Tukey's multiple comparisons test. (B) Representative LV M-mode long-axis echocardiography views at end-diastole on day 0 and day 28 post-MI in MT1-MMP$^{f/f}$ and MT1-MMP$^{\Delta LysM}$ mice. (C, D) Post-MI progression of LVEF and LVVold (C) and infarct size (percentage of LV with contractility alterations) and WMSI (D) assessed by echocardiography. Data are means ± SEM of 9-10 mice per genotype. Two-way ANOVA followed by Tukey's multiple comparisons test. (E) Quantitative assessment of LV contractility at 28 days post-MI, showing mean scores for every LV segment at the basal, medial, and apical levels throughout all samples. L, lateral; A, anterior; P, posterior; S, septal. Segment scores are colored-coded from green to red: green = normal, yellow = hypokinesia, orange = akinesia, and red = dyskinesia or aneurysm. (F) Representative SHG (white) and MPEF (green) microscopy images of transverse cardiac sections at 28 days post-MI. Scale bar, 500 µm. Magnified views of boxed areas within the infarct are shown in the lower panels. Scale bar, 100 µm. Asterisks mark the epicardium. (G) Percentage SHG, skewness, and kurtosis in infarcts at 28 days post-MI. Data are means ± SEM of 5-7 mice per genotype. Unpaired *t*-test.

Figure 2. MT1-MMP$^{\Delta LysM}$ mice have a preserved microvasculature network and better myocardial oxygenation after ischemic injury. (A) Representative confocal microscopy images showing immunostaining for CD31 (green) and nuclei (blue) within the infarction in MT1-MMP$^{f/f}$ and MT1-MMP$^{\Delta LysM}$ hearts at 7 days post-MI. Scale bar, 50 µm. (B) Vasculature-related parameters within the infarction at 7 days post-MI. Data are means ± SEM of 5-6 mice per genotype. Unpaired *t*-test. (C) Representative confocal immunofluorescence microscopy images of CA-IX (red) in the infarcted region of MT1-MMP$^{f/f}$ and MT1-MMP$^{\Delta LysM}$ hearts at 7 days post-MI. Nuclei are stained with DAPI (blue). Scale bar, 100 µm. (D) CA-IX^{+} area:total area ratio in the infarcted zone. Data are means ± SEM of 7-8 mice per genotype. Unpaired *t*-test.

Figure 3. Mφ-deletion of MT1-MMP impairs active TGFβ1 release from LAP-TGFβ1 complex. (A) Scheme of LAP-TGFβ1 complex retention in the cell surface through LAP-binding to membrane receptors. (B) Representative flow cytometry histogram plots of LAP and TGFβ1 staining in LPS-activated MT1-MMP$^{f/f}$ and MT1-MMP$^{\Delta LysM}$ BMDMs. (C) Standardized mean fluorescence intensity (MFI) of LAP and TGFβ1 in experiments as in B. Data are means ± SEM of 7 mice per group. Unpaired *t*-test. (D) Western blot of transferrin receptor (TfR), α-

tubulin, and LAP-TGFβ1 complex in membrane fraction (Mb), cytosolic fraction (C), and total lysate (T) from LPS-activated MT1-MMP$^{f/f}$ and MT1-MMP$^{\Delta LysM}$ BMDMs. (E) Quantification of LAP-TGFβ1 complex in the membrane fraction. Data are means ± SEM of 6-7 mice per genotype. Unpaired *t*-test. (F) *Tgfb1* mRNA expression in LPS-activated MT1-MMP$^{f/f}$ and MT1-MMP$^{\Delta LysM}$ BMDMs. Data are means ± SEM of 5 mice per genotype. Unpaired *t*-test. (G) Arbitrary luciferase units (ALU) in HEK293 cells co-cultured with or without LPS-activated MT1-MMP$^{f/f}$ or MT1-MMP$^{\Delta LysM}$ BMDMs. Control corresponds to transfected HEK293 cells cultured alone. Data are means ± SEM of a representative experiment of three performed with four technical replicates per condition. One-way ANOVA followed by Tukey's multiple comparisons test. (G) ALU in HEK293 cells co-cultured with or without conditioned media from LPS-activated MT1-MMP$^{\Delta LysM}$ BMDMs transduced with mock lentivirus (GFP), or lentivirus containing full-length MT1-MMP (FL) or catalytic MT1-MMP mutant (E240A). Control corresponds to transfected HEK293 cells cultured alone. Data are means ± SEM of a representative experiment of three performed with three technical replicates per condition. One-way ANOVA followed by Tukey's multiple comparisons test.

Figure 4. The absence of Mφ MT1-MMP reduces TGFβ1-pSMAD2 signaling in cardiac ECs, MyoFBs, and VSMCs after MI. (A) Gating strategy used to assess pSMAD2 signaling in ECs, MyoFBs/VSMCs, and Mφs. (B) Representative flow cytometry histogram plots of pSMAD2 staining in the indicated cells from 7-day-post-MI hearts. (C) Standardized MFI of pSMAD2 in experiments as in B. Data are means ± SEM of 7-8 mice per genotype. Unpaired *t*-test. (D) Representative immunofluorescence staining of CD31 (green), SMA (red), and pSMAD2 (white) in infarcted cardiac tissue from MT1-MMP$^{f/f}$ mice (top) and MT1-MMP$^{\Delta LysM}$ mice (bottom) at 7 days post-MI. Nuclei are stained with DAPI (blue). Red and yellow arrowheads point to pSMAD2^{+} MyoFBs and pSMAD2^{+} VSMCs, respectively. Scale bar, 50 μm. (E) Percentages of pSMAD2^{+} MyoFBs and pSMAD2^{+} VSMCs within the total MyoFB or VSMC populations, respectively in the infarcted zone. Data are means ± SEM of 6 mice per genotype. Unpaired *t*-test.

Figure 5. The absence of Mφ MT1-MMP alters myocardial cellular composition after MI. (A) Flow cytometry gating strategy used to identify and quantify cardiac ECs, MyoFBs, cells undergoing EndMT, and Mφs in MT1-MMP$^{f/f}$ mice (left) and MT1-MMP$^{\Delta LysM}$ mice (right) on day 7 after MI. (B) Quantification of Mφs, ECs, MyoFBs, and cells undergoing EndMT in cardiac tissue 7 days after MI. Data are means ± SEM of at least 11 mice per genotype. Unpaired *t*-test.

Figure 6. Cardiac Mφs induce post-MI EndMT through MT1-MMP-mediated TGFβ1 activation. (A) Standardized MFI of LAP and TGFβ1 staining in MT1-MMP$^{f/f}$ and MT1-MMP$^{\Delta LysM}$ cardiac Mφs on day 7 after MI. Data are means ± SEM of 6-7 mice per group.

Unpaired *t*-test. (B) Luciferase activity (ALU) in transfected HEK293 cells co-cultured with Mφs from 7-day-post-MI MT1-MMP$^{f/f}$ or MT1-MMP$^{\Delta LysM}$ hearts. Data are means ± SEM of three independent experiments performed with four technical replicates per condition. One-way ANOVA followed by Tukey's multiple comparisons test. (C) Representative immunofluorescence staining of CD31 (green) and SMA (red) in *in vitro* co-cultures of MAECs and cardiac Mφs from MT1-MMP$^{f/f}$ or MT1-MMP$^{\Delta LysM}$ 7-day-post-MI hearts. Nuclei are stained with DAPI (blue). Scale bar, 100 µm (D) CD31^{+} area (µm^2) and SMA^{+} area (µm^2) in the different conditions. Data are means ± SEM of a representative experiment of three performed with three technical replicates per condition. Unpaired *t*-test.

Figure 7. Mφ-deletion of MT1-MMP preserves cardiac function after MI by impairing TGFβ1-mediated EndMT. MI triggers MT1-MMP production by Mφs, contributing to release of active TGFβ1 from SLC (LAP-TGFβ1) to the myocardium. Active TGFβ1 signals acting on ECs promote EndMT, contributing to adverse tissue remodeling. When Mφ MT1-MMP is absent, latent TGFβ1 accumulates, and the availability of active TGFβ1 in the myocardium decreases. In this scenario, the impairment of Mφ-mediated EndMT results in enhanced angiogenesis and reduced fibrosis, limiting LV remodeling and preserving cardiac function.

Video 1. Parasternal 2D long axis echocardiography view of MT1-MMP$^{f/f}$ or MT1-MMP$^{\Delta LysM}$ hearts at baseline (Day 0) and at 28 days post-MI induced by LAD-ligation.

Figure 1

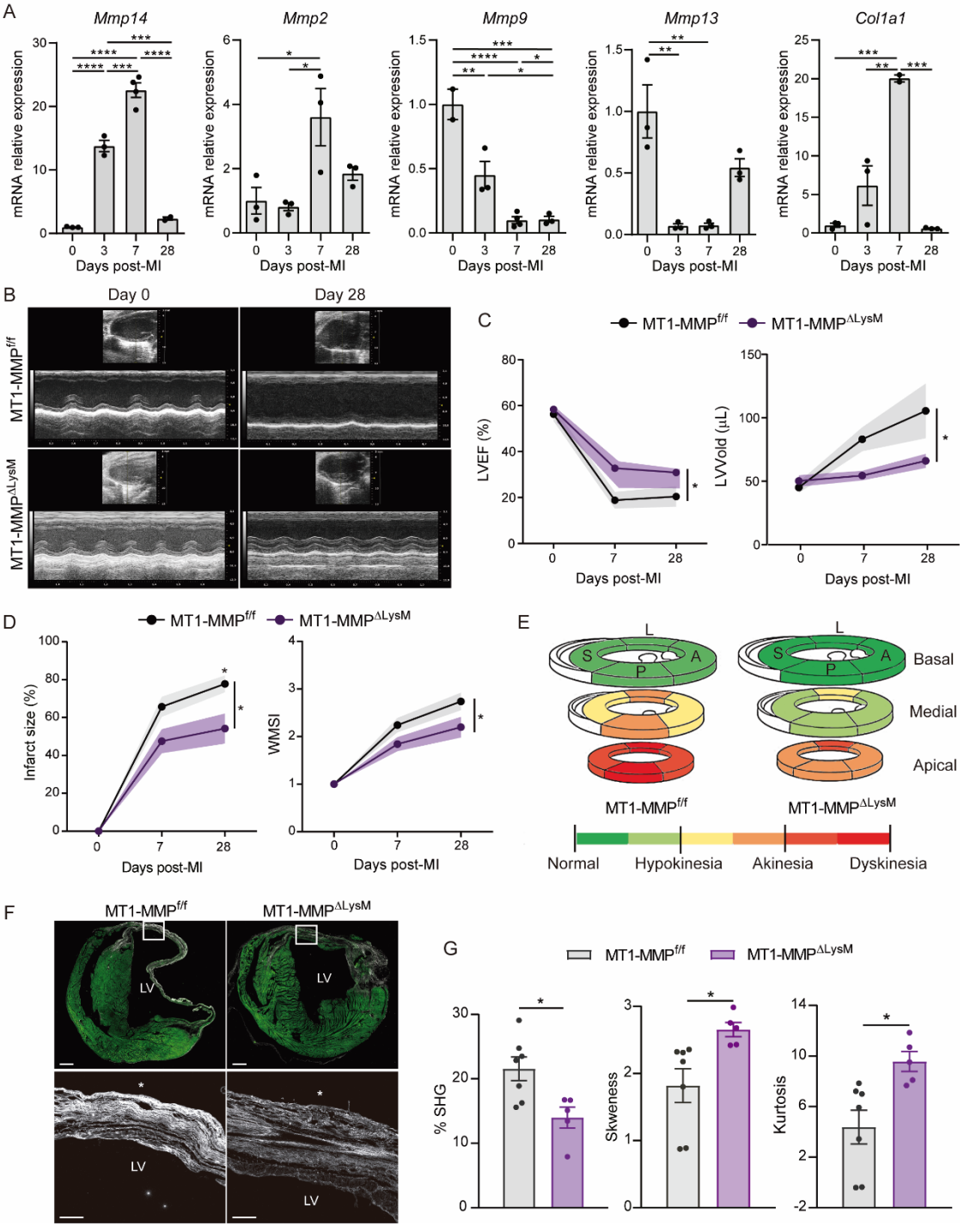

1024

Figure 2

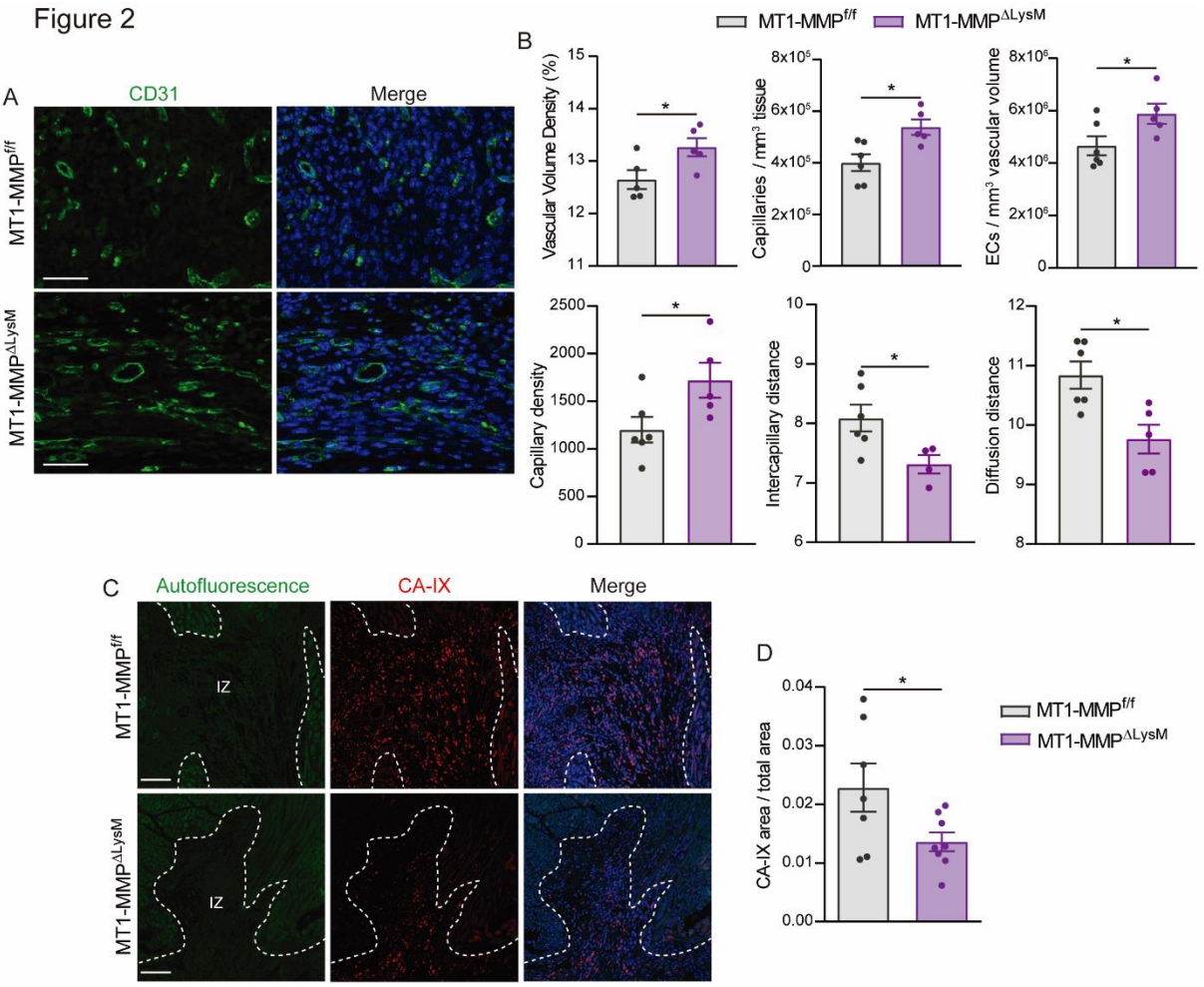

1025

Figure 3

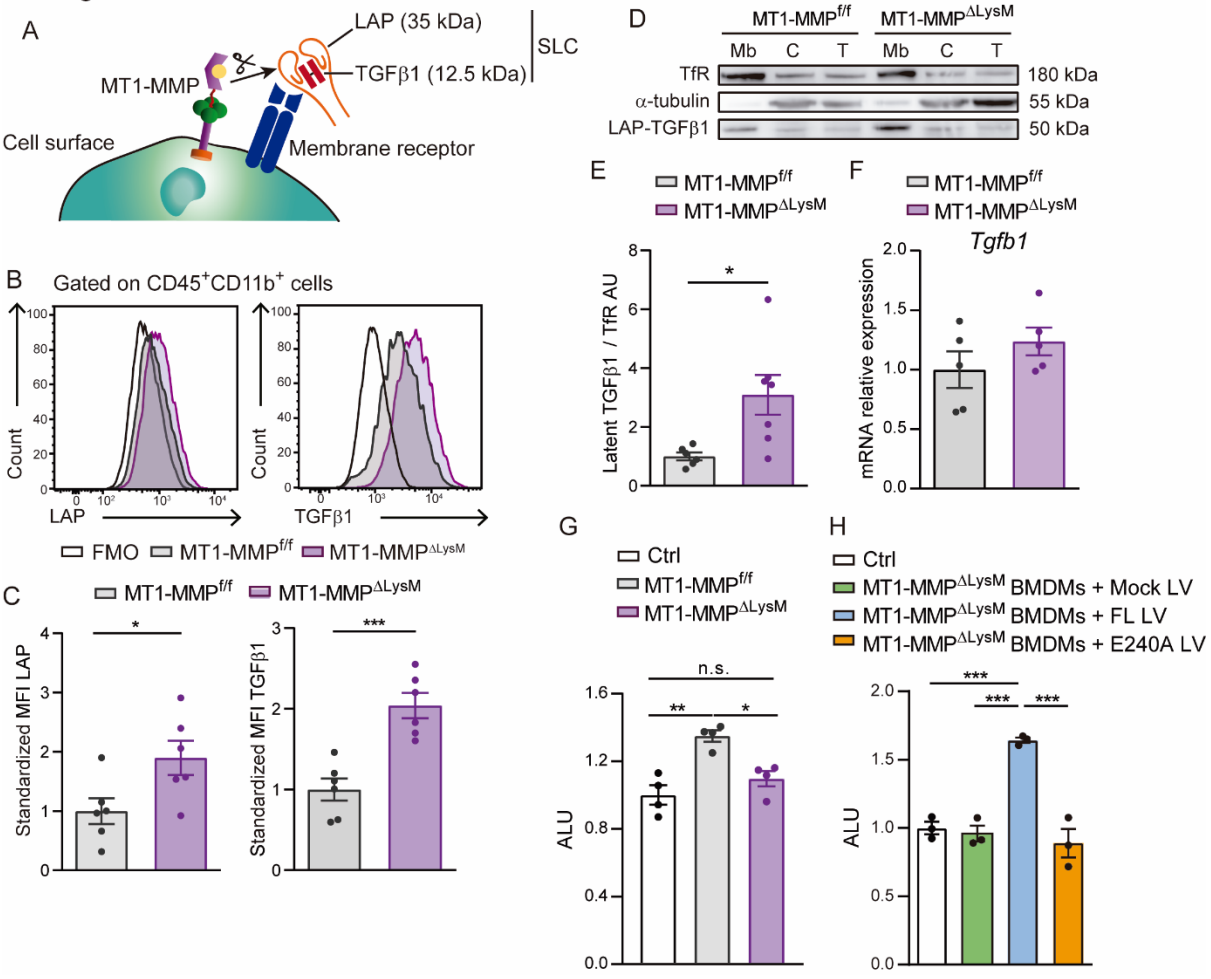

1026

Figure 4

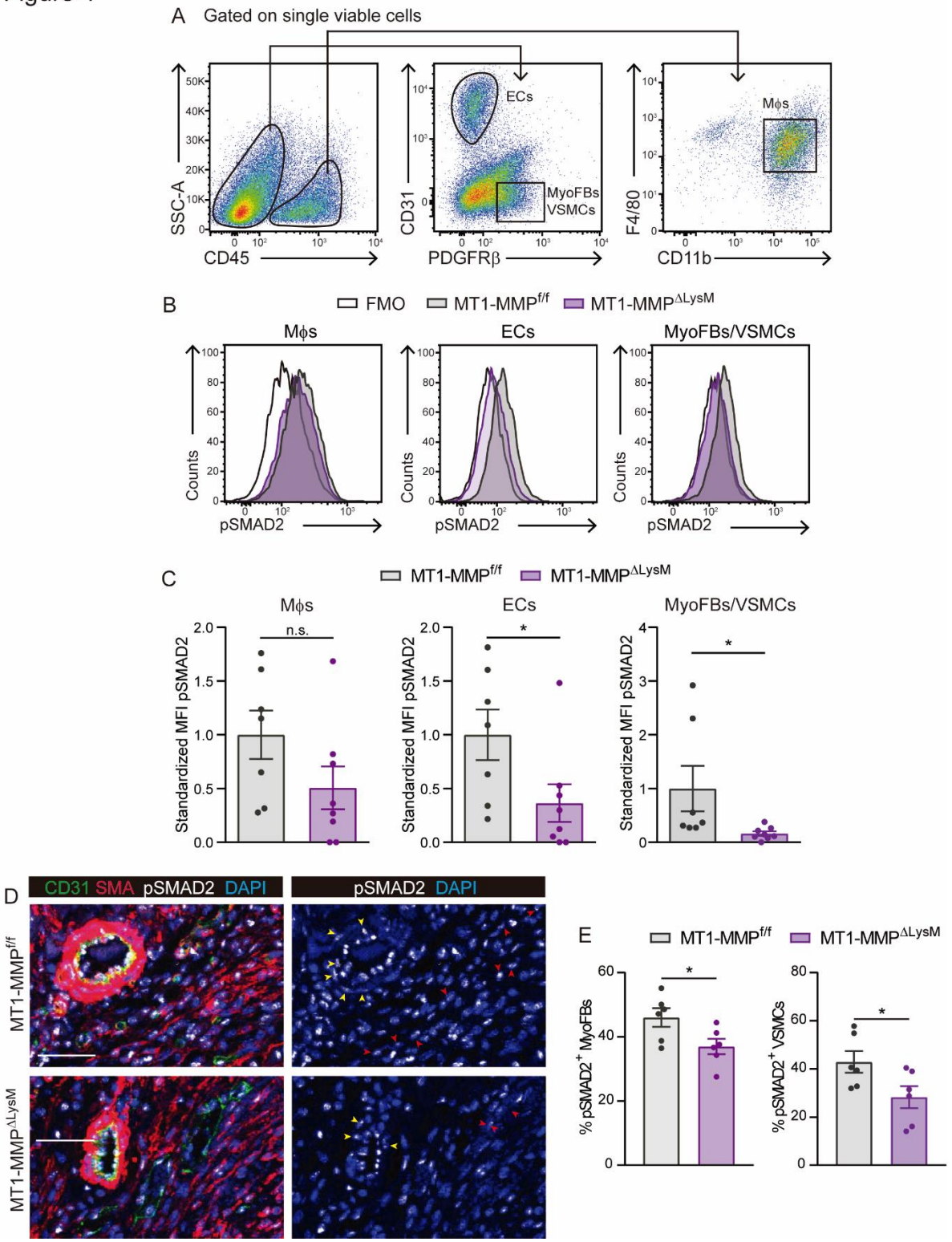

1027

Figure 5

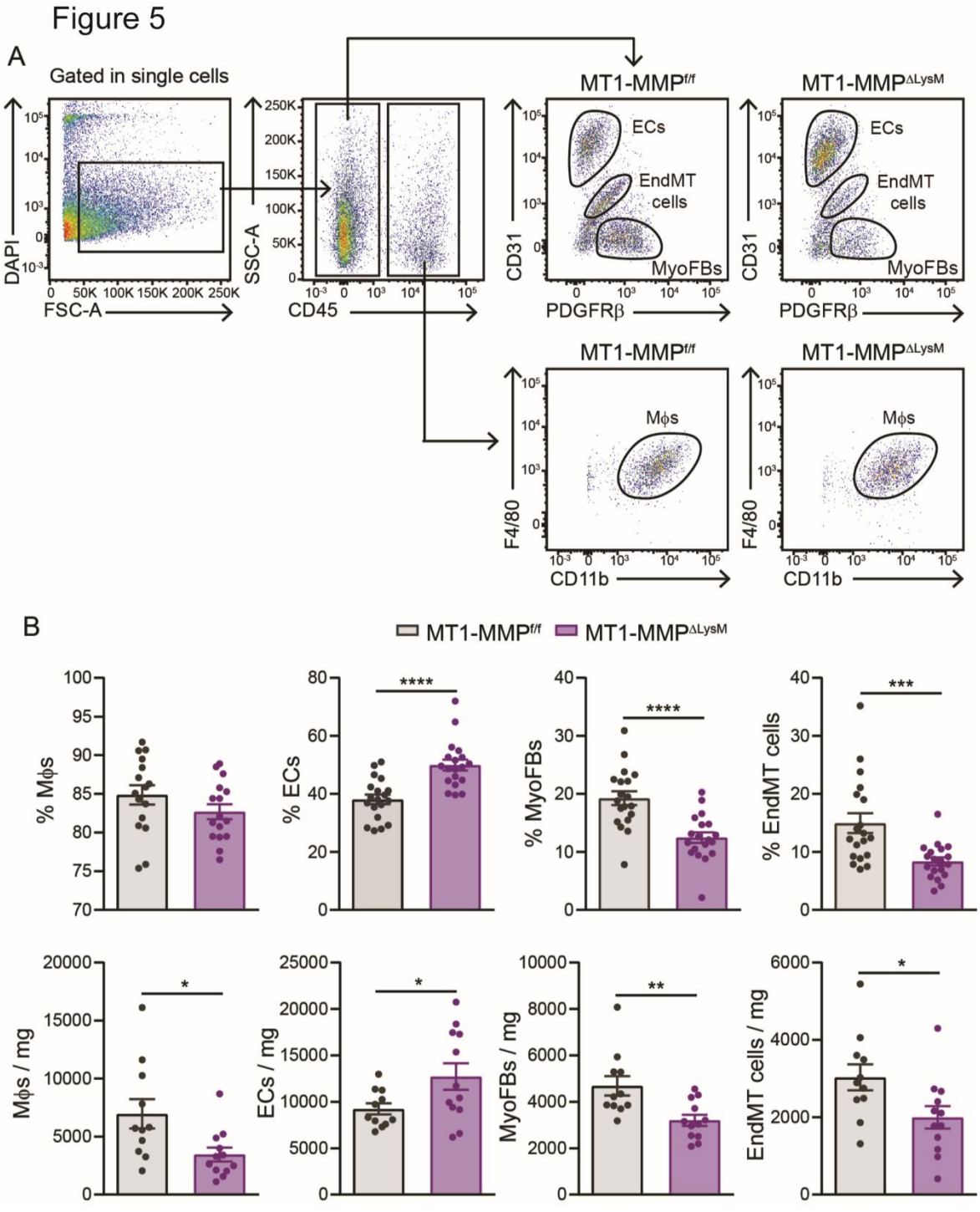

1028

Figure 6

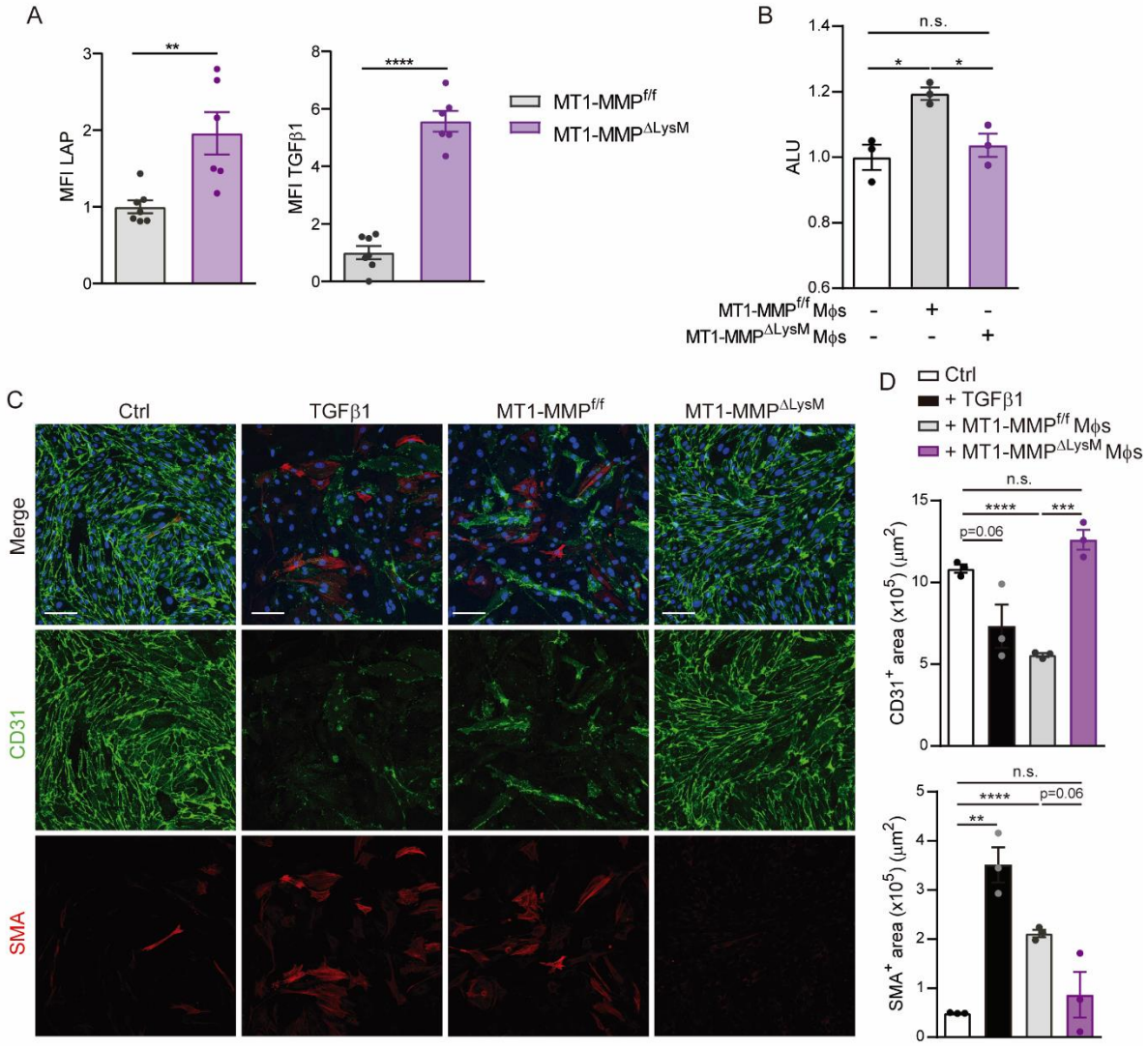

1029

Figure 7

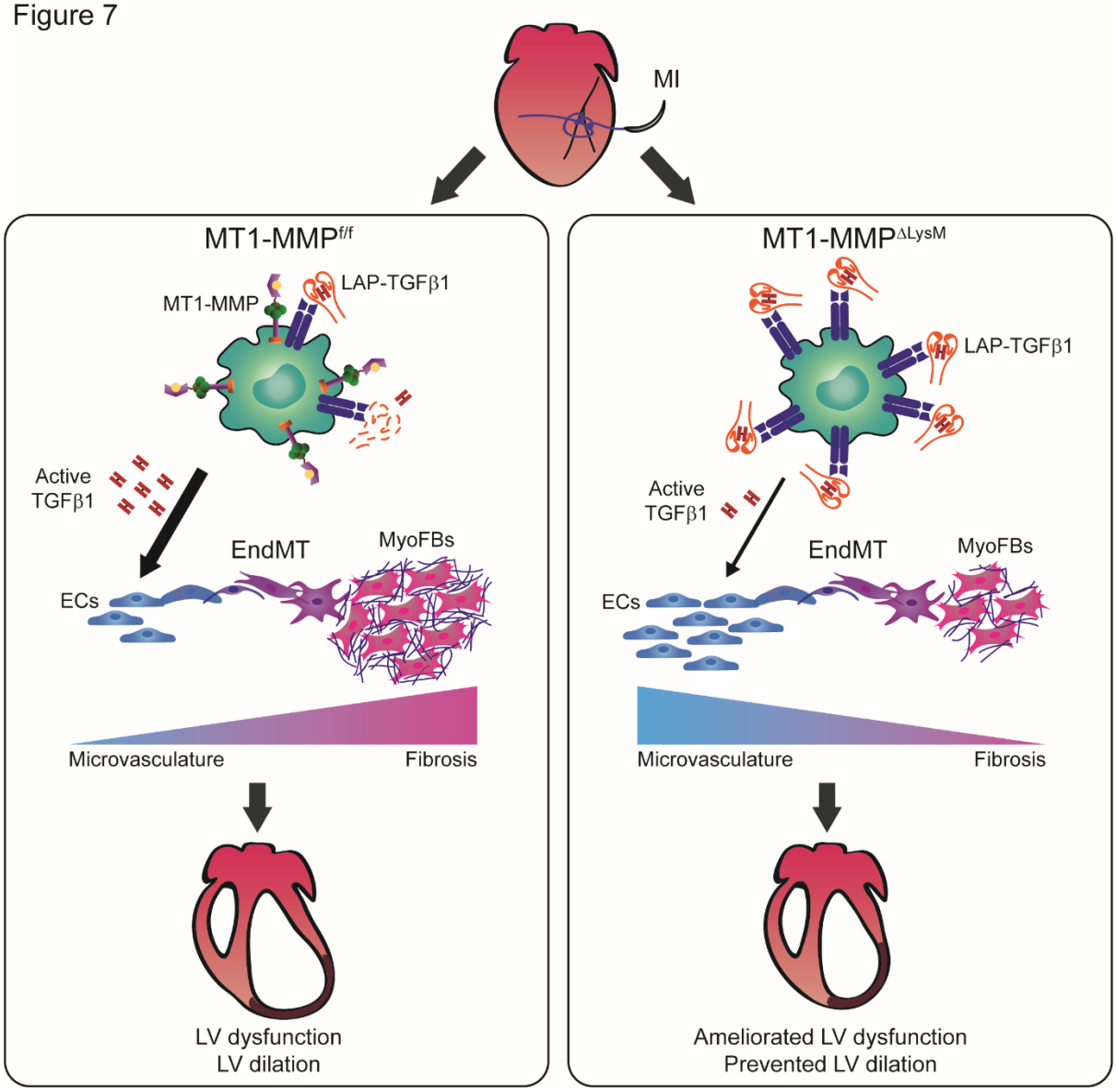

1030

SUPPLEMENTAL FIGURES AND FIGURE LEGENDS

Figure 1- Figure supplement 1. Isolation of cardiac Mφs after MI. (A) FACS gating strategy to purify cardiac Mφs from C57BL/6 mice. (B) From the myeloid cell population ($CD45^+CD11b^+$ cells), $F4/80^+Ly6C^{low}$ cells (blue) were isolated at 0, 7, and 28 days post-MI, and F4/80+/$Ly6C^{high}$ cells (red) were purified at 3 days post-MI. Representative post-sort plots of Mφs are shown in the lower panel. Sorting was performed with a pool of 3-5 mice per time point.

Figure 1- Figure supplement 2. Mouse model of Mφ-specific MT1-MMP deletion. (A) Strategy for generating the transgenic mouse line used for Mφ deletion of *Mmp14.* LoxP sites (red arrowheads) were introduced flanking exons 4 and 5, and a FRT-PGK-Neo-FRT-cassette was inserted between exons 5 and 6 to generate the *Mmp14*$^{f/f}$ construct (top, right). To obtain Mφ deletion of *Mmp14*, MT1-MMP$^{f/f}$ mice were crossed with LysM-Cre mice, yielding the floxed *Mmp14* allele (bottom, right) in MT1-MMP$^{\Delta LysM}$ mice. Green rectangles indicate alignment position for genotyping primers. (B) Representative plots showing the gating strategy for the identification of circulating monocytes ($CD45^+CD11b^+Ly6G^-CD115^+Ly6C^{high}$ cells) and neutrophils ($CD45^+CD11b^+Ly6G^+CD115^-Ly6C^{low}$ cells) in peripheral blood from MT1-MMP$^{f/f}$ and MT1-MMP^{DLysM} mice. (C) Total numbers of baseline circulating monocytes and neutrophils as depicted in B. Data are means ± SEM of 9-10 mice per genotype. (D) qPCR analysis of *Mmp14* deletion efficiency in BMDMs and FACS-sorted 7-day-post-MI cardiac Mφs ($CD45^+CD11b^+F4/80^+Ly6C^{low}$ cells) and ECs ($CD45^-CD11b^-CD31^+$ cells) from MT1-MMP$^{f/f}$ and MT1-MMP$^{\Delta LysM}$ mice. Data are means ± SEM of 7 mice per genotype (for BMDMs) or 4-6 independent pools of 2 mice per genotype (for cardiac Mφs and cardiac ECs). Unpaired *t*-test.

Figure 1- Figure supplement 3. The absence of Mφ MT1-MMP ameliorates cardiac dysfunction and reduces collagen deposition in a model of transient ischemia. (A) Progression of LVEF, LVIDs, and LVIDd in MT1-MMP$^{f/f}$ and MT1-MMP$^{\Delta LysM}$ mice after ischemia/reperfusion (I/R). Data are means ± SEM of 14 mice per genotype. Two-way ANOVA followed by Tukey's multiple comparisons test. (B) Representative SHG (white) and MPEF (green) microscopy images of transverse cardiac sections from MT1-MMP$^{f/f}$ and MT1-MMP$^{\Delta LysM}$ mice at 21 days after I/R. Scale bar, 1 mm. Magnified views of boxed areas in the infarct are shown in the lower panels. Scale bar, 100 µm. (C) Percentage SHG, skewness, and kurtosis in infarcts at 21 days post-I/R. Data are means ± SEM of 5-7 mice per genotype. Unpaired *t*-test.

Figure 2- Figure supplement 1. Remodeling of cardiac vasculature in MT1-MMP$^{\Delta LysM}$ mice after MI. (A) Representative confocal immunofluorescence microscopy images of CA-IX (red) in MT1-MMP$^{f/f}$ and MT1-MMP$^{\Delta LysM}$ hearts at 7 days post-MI in the remote zone (RZ).

Nuclei are stained with DAPI (blue). Scale bar, 100 µm. (B) CA-IX^{+} area:total area ratio in the RZ. Data are means ± SEM of 7-8 mice per genotype. Unpaired *t*-test. (C) Representative images of SMA-stained transverse sections of MT1-MMP$^{f/f}$ and MT1-MMP$^{\Delta LysM}$ hearts at 7 days post-MI. Scale bar, 1 mm. Magnified views of boxed areas in the infarct are shown on the right. Scale bar, 100 µm. (D) SMA^{+} vessel density and SMA^{+} vessel wall thickness in the IZ at 7 days post-MI. Data are means ± SEM of 5-7 per group. Unpaired *t*-test.

Figure 5- Figure supplement 1. Endothelial-to-mesenchymal gene signature of CD31^{+}PDGFRβ^{+} cells. (A) FACS gating strategy to purify cardiac ECs, EndMT cells, and MyoFBs/VSMCs from 7 days post-MI WT hearts. Representative post-sort plots of Mφs are shown in the lower panel. Sorting was performed with a pool of 2 mice per time point. (B) qPCR analysis of ECs, EndMT cells, and MyoFBs/VSMCs for endothelial genes (*Pecam, Cdh5, Kdr, Col4a1, Col4a2*) and fibroblast genes (*Cdh2, Tagln, Col1a1, Col1a2, Col3a1*), and EndMT-mediating transcription factors (*Zeb2* and *Snai1*). Data are means ± SEM of at least three independent biological replicates per group. Two-way ANOVA followed by Tukey's multiple comparisons test.

Figure 5- Figure supplement 2. Lineage tracing of endothelial derived-mesenchymal cells. (A-E) Representative flow cytometry plots showing expression of Tomato and PDGFRβ in CD45- cardiac cells in the indicated mice. (A) C57BL/6 FMO sample for PDGFRβ; (B) C57BL/6 sample stained with anti-PDGFRβ antibody; (C) VE-Cadh-Cre^{ERT2} R26Tomato FMO sample for PDGFRβ; (D, E) Cdh5-Cre^{ERT2} R26Tomato sample stained with anti-PDGFRβ antibody in control (D) or 7 day-post-MI hearts (E). Numbers indicate percentage of cells within the CD45- cell population. Representative plots of n=2 hearts per condition.

Figure 5- Figure supplement 3. The absence of Mφ MT1-MMP attenuates post-MI EndMT. (A) Complementary flow cytometry gating strategy used to identify and quantify cardiac ECs, MyoFBs/VSMCs, and cells undergoing EndMT in MT1-MMP$^{f/f}$ mice (left) and MT1-MMP$^{\Delta LysM}$ mice (right) on day 7 after MI. (B) Quantification of ECs, MyoFBs, and cells undergoing EndMT in cardiac tissue 7 days after MI. Data are means ± SEM of 7-8 mice per genotype. Unpaired *t*-test. (C) Representative confocal immunofluorescence microscopy images of pSMAD2 (green), SMA (red), ERG (white) and DAPI (blue) of the infarcted area of MT1-MMP$^{f/f}$ hearts at 7 days post-MI. Arrows indicate ERG^{+}/SMA^{+}/pSMAD2^{+} cells, asterisks indicate ERG^{+}/SMA^{-}/pSMAD2^{+} cells, and arrowheads indicate ERG^{-}/SMA^{+}/pSMAD2^{+} cells. Scale bar, 50 µm. (D) Triple positive cells named “a” and “b” are shown magnified with their orthogonal views in the boxes to the right. Scale bar, 5 µm.

Figure 6- Figure supplement 1. MT1-MMP is required for *in vitro* Mφ induction of EndMT. (A) Representative immunofluorescence staining of CD31 (green) and SMA (red) in *in vitro*

co-cultures of MAECs and LPS-activated MT1-MMP$^{f/f}$ or MT1-MMP$^{\Delta LysM}$ BMDMs. Nuclei are stained with DAPI (blue). MAECs were also treated with TGFβ1 (10 ng/ml) as an EndMT positive control. Scale bar, 100 µm (B) CD31^{+} area (µm^2) and SMA^{+} area (µm^2) in the different conditions. Data are means ± SEM of four independent experiments carried out with three technical replicates per condition. Unpaired *t*-test. (C) qPCR analysis of endothelial and myofibroblast markers and TGFβ1 target genes in *in vitro* co-cultures of MAECs and LPS-activated MT1-MMP$^{f/f}$ or MT1-MMP$^{\Delta LysM}$ BMDMs. Data are means ± SEM of a representative experiment of two performed with three technical replicates per condition. Unpaired *t*-test.

Figure 1 - Figure Supplement 1

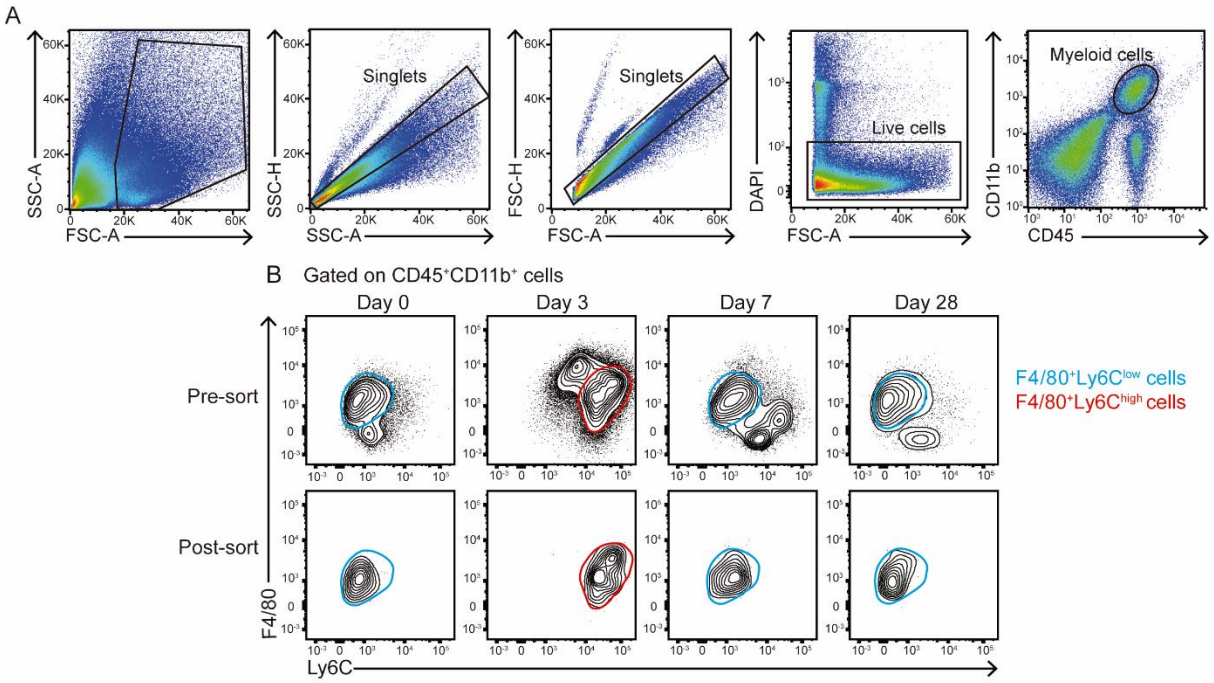

1109

Figure 1- Figure supplement 2

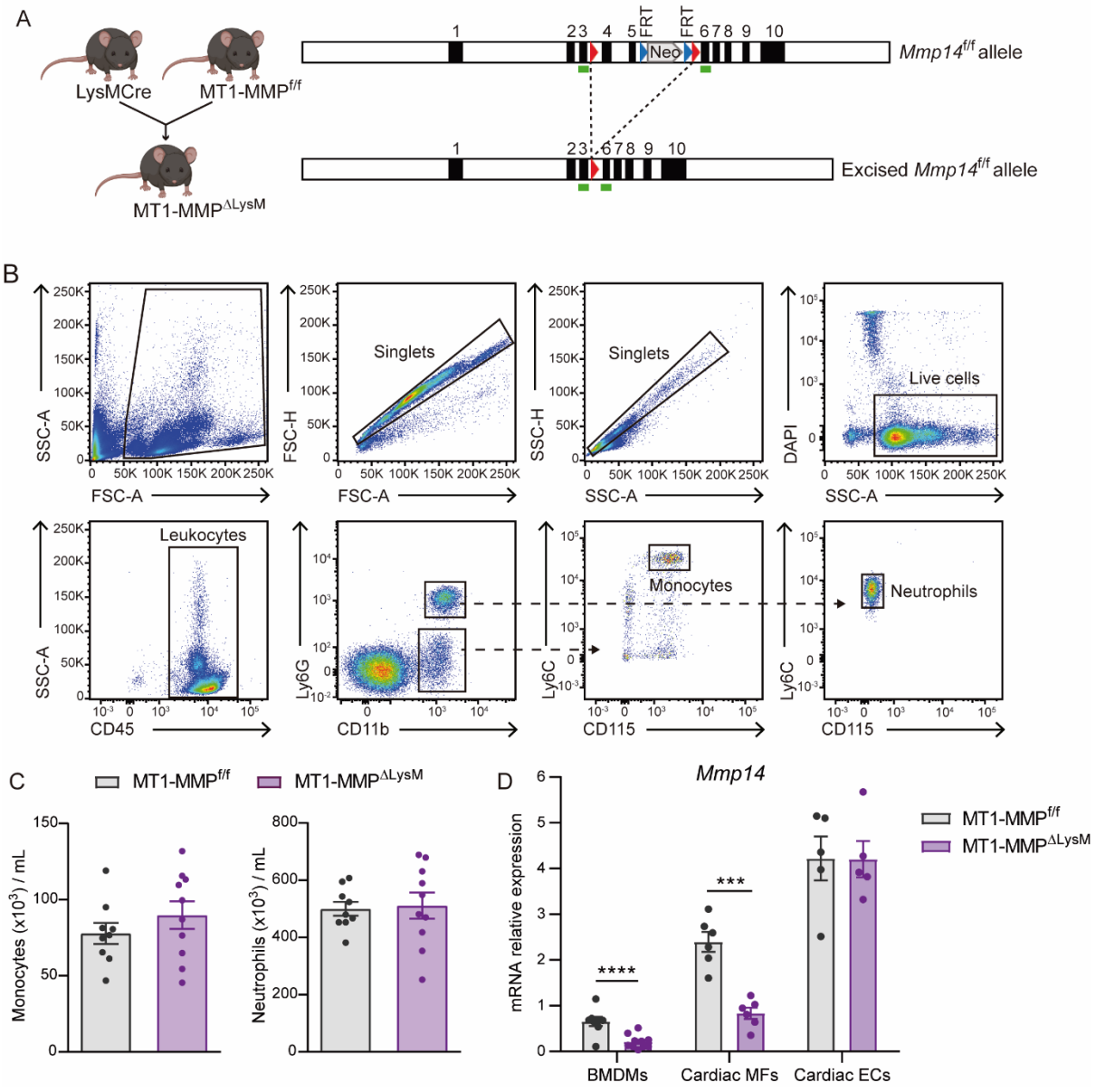

1110

Figure 1- Figure supplement 3

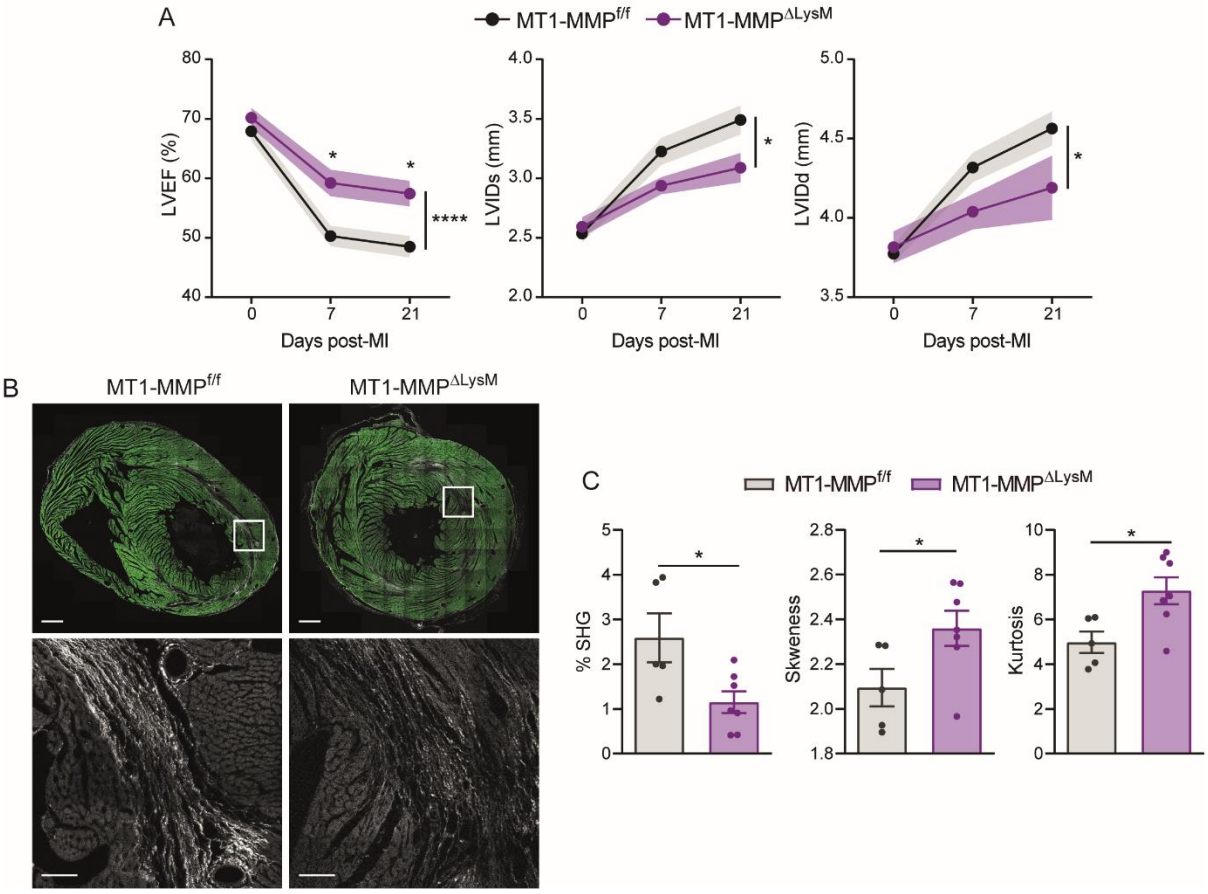

1111

Figure 2- Figure supplement 1

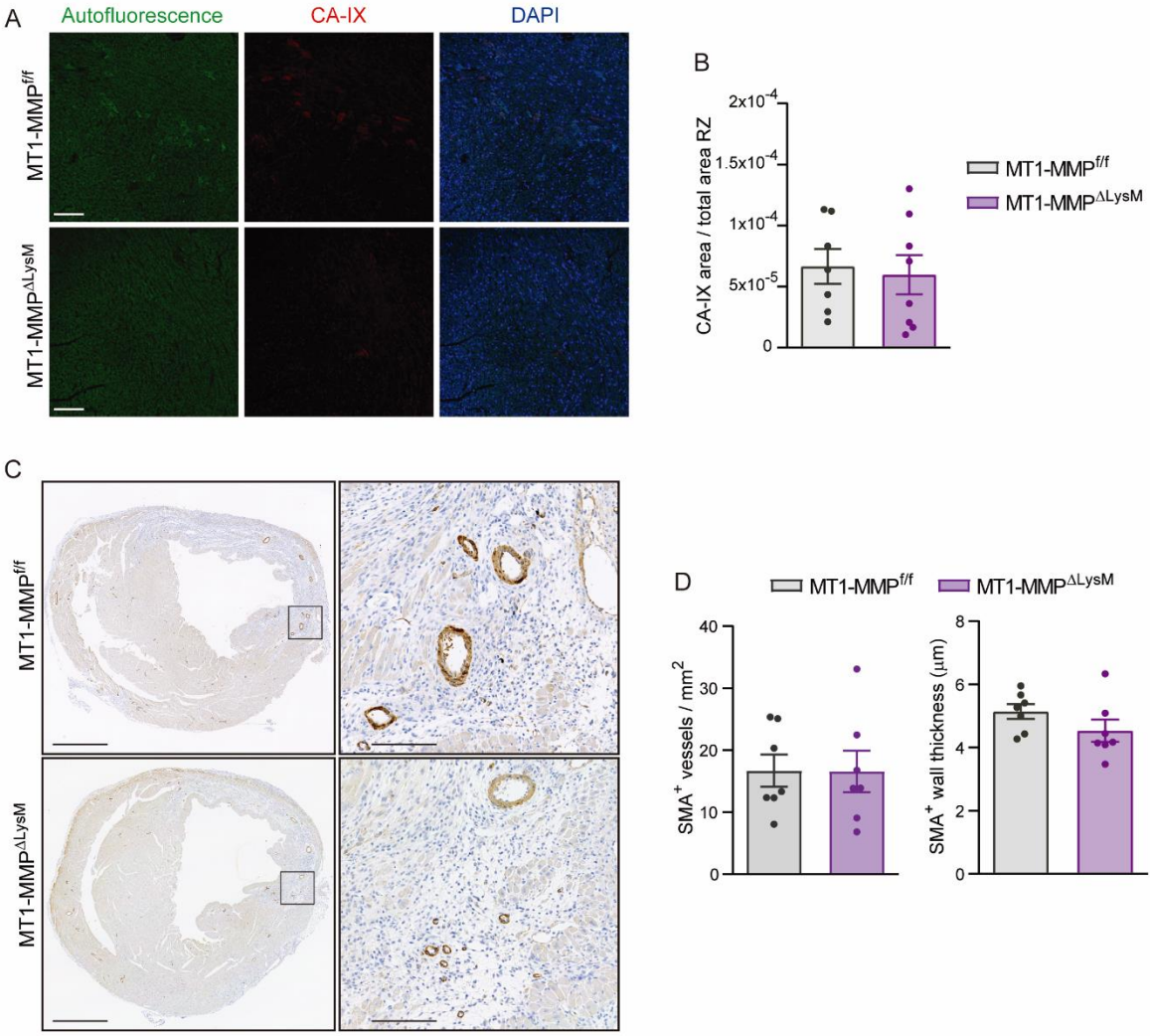

1112

Figure 5 - Figure supplement 1

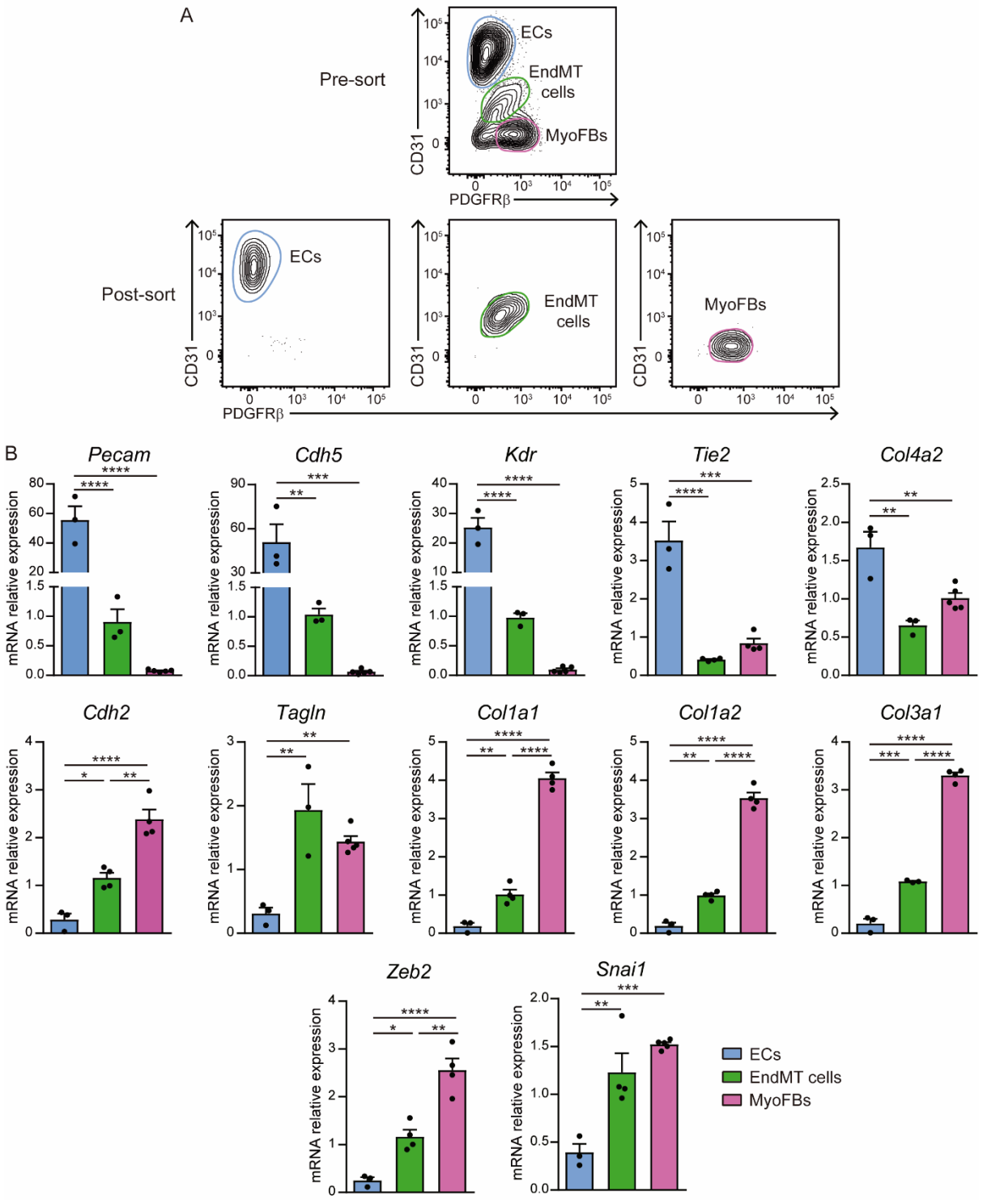

1113

Figure 5 - Figure Suplement 2

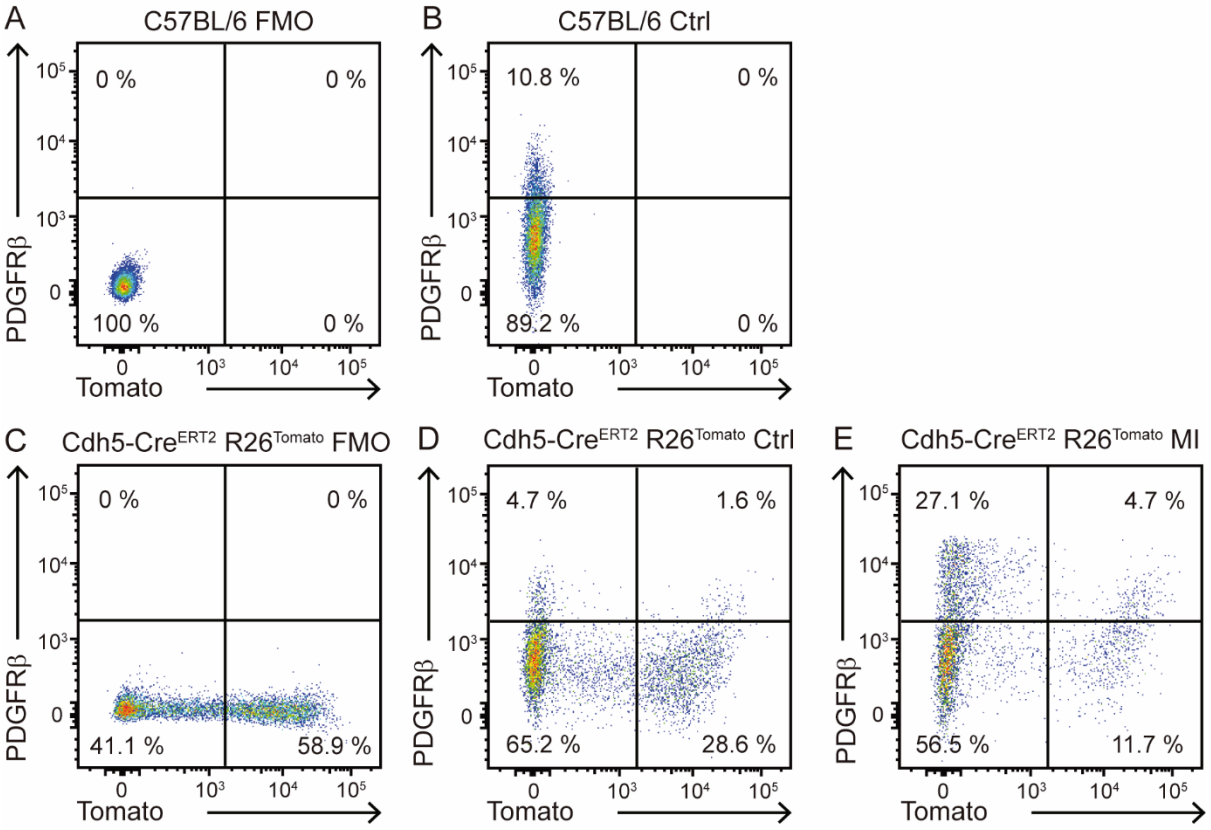

1114

Figure 5 - Figure Supplement 3

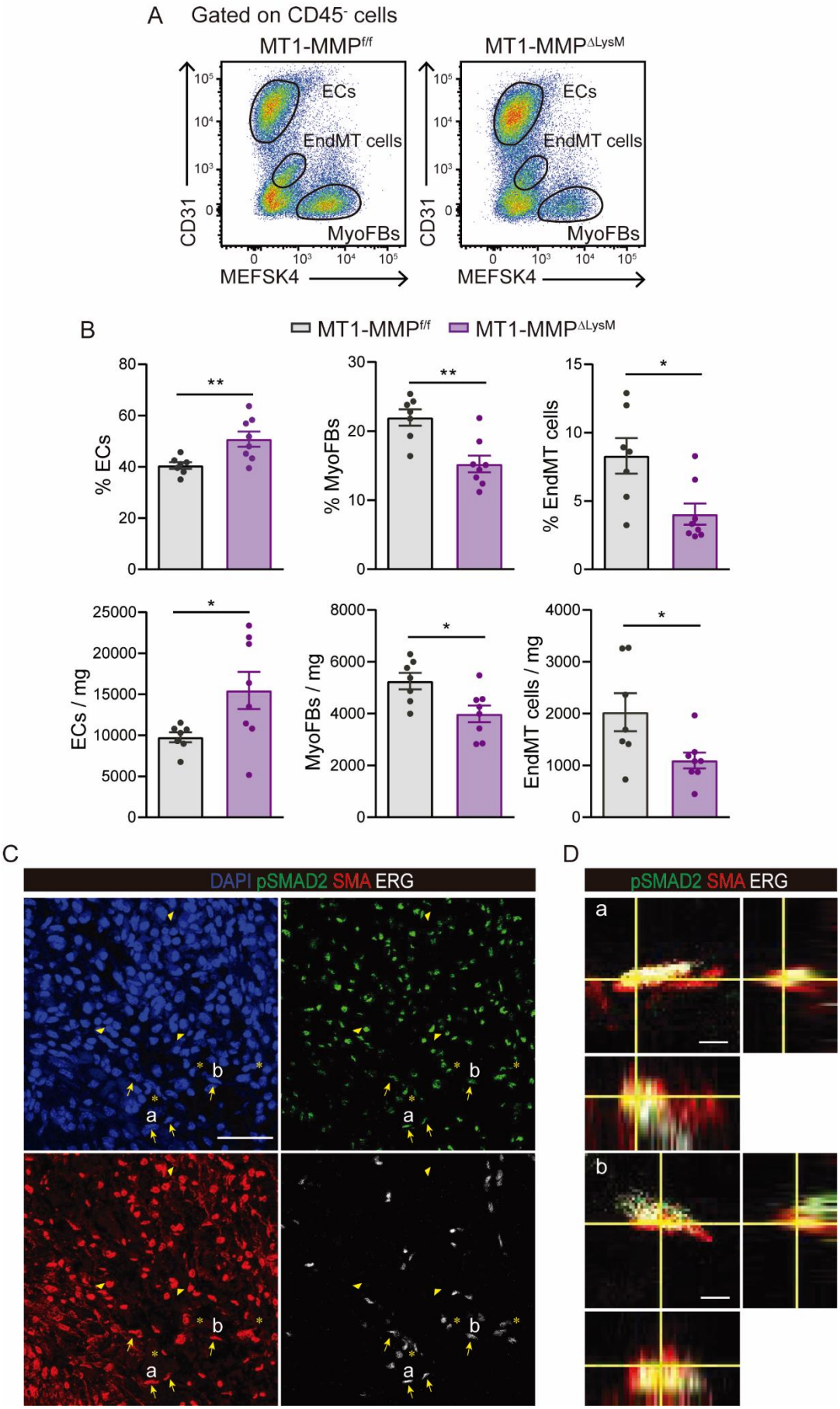

Figure 6 - Figure Supplement 1

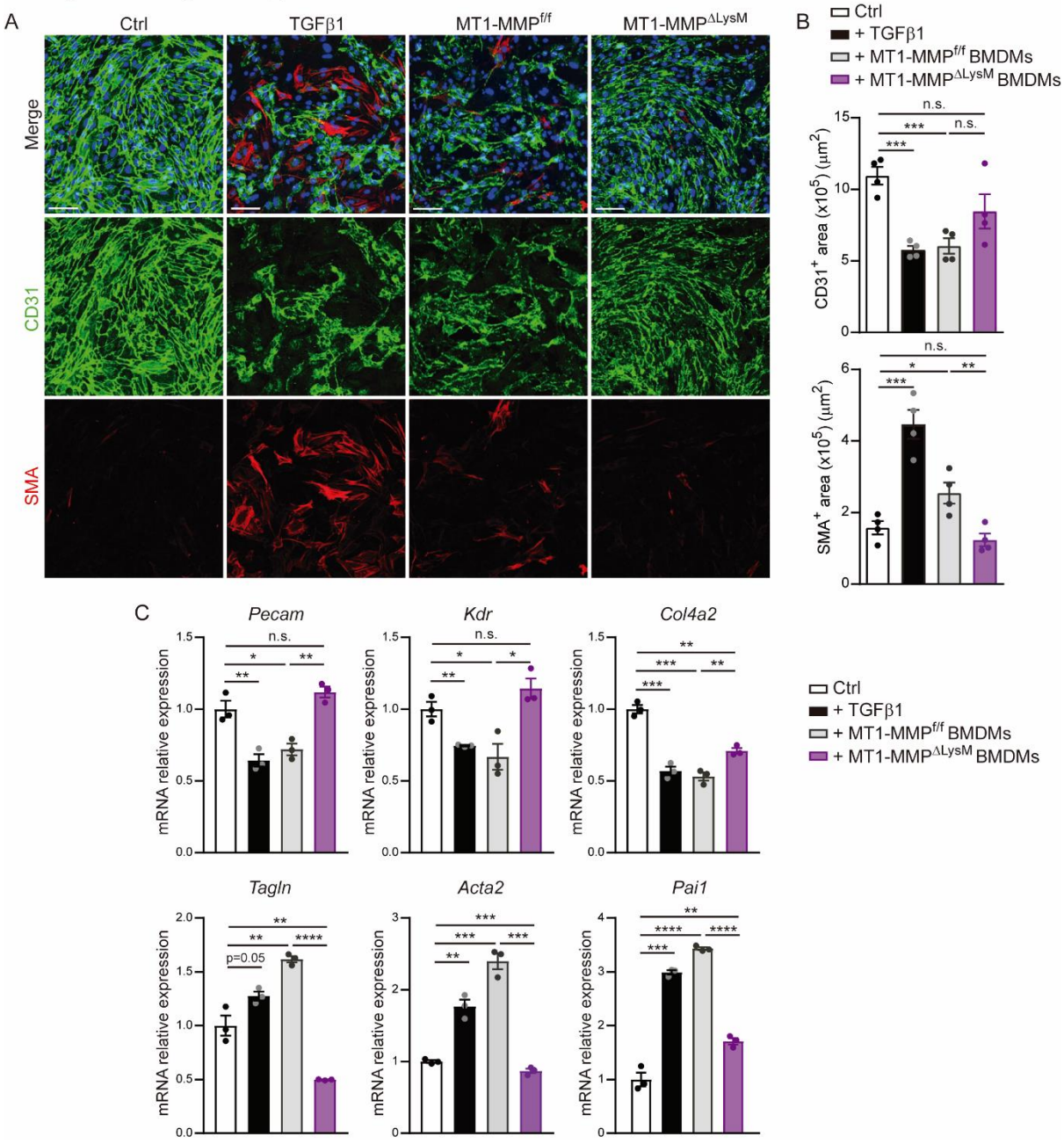

1116